

Supersymmetric quantum mechanics on the lattice: II. Exact results

David Baumgartner and Urs Wenger

Albert Einstein Center for Fundamental Physics,
Institute for Theoretical Physics, University of Bern,
Sidlerstrasse 5, CH-3012 Bern, Switzerland

Abstract

Simulations of supersymmetric field theories with spontaneously broken supersymmetry require in addition to the ultraviolet regularisation also an infrared one, due to the emergence of the massless Goldstino. The intricate interplay between ultraviolet and infrared effects towards the continuum and infinite volume limit demands careful investigations to avoid potential problems. In this paper – the second in a series of three – we present such an investigation for $\mathcal{N} = 2$ supersymmetric quantum mechanics formulated on the lattice in terms of bosonic and fermionic bonds. In one dimension, the bond formulation allows to solve the system exactly, even at finite lattice spacing, through the construction and analysis of transfer matrices. In the present paper we elaborate on this approach and discuss a range of exact results for observables such as the Witten index, the mass spectra and Ward identities.

1 Introduction

Regularising supersymmetric quantum field theories on a lattice in order to investigate their nonperturbative properties remains to be a challenging and demanding task. Besides the fact that the discreteness of the space-time lattice explicitly breaks the Poincaré symmetry, and hence supersymmetry itself, it can also be broken by specific choices of the boundary conditions, in particular also by the finite temperature. As a consequence, the effects from the ultraviolet and infrared lattice regularisation are sometimes difficult to separate from each other. In addition, the restoration of supersymmetry in the continuum and infinite volume limit is in general a delicate process which requires careful fine-tuning or highly involved discretisation schemes, both of which are sometimes difficult to control. For these reasons a complete and thorough understanding of the intricate interplay between infrared and ultraviolet effects, when removing the corresponding lattice regulators, is a crucial prerequisite for any investigation of supersymmetric field theories on the lattice.

Supersymmetric quantum mechanics is a simple system which nevertheless contains many of the important ingredients characterising supersymmetric field theories. Moreover, in the path integral formalism the system differs little from field theories in higher dimensions and it is sufficiently involved to show similar complexity and complications. Hence, supersymmetric

quantum mechanics provides an adequate playground to address all the delicate questions and issues mentioned above. In this paper – the second in a series of three – we present exact results for $\mathcal{N} = 2$ supersymmetric quantum mechanics discretised on the lattice using the bond formulation. This formulation is based on the hopping expansion of the original bosonic and fermionic degrees of freedom and is described in detail in the first paper of our series [1]. For the fermions the bond formulation is more appropriately termed fermion loop formulation since the fermionic bond configurations turn out to be closed fermionic loops. In the case of $\mathcal{N} = 2$ supersymmetric quantum mechanics the fermion loop formulation is particularly simple, since there are only two different fermion loop configurations, namely one containing exactly one fermion loop winding around the lattice in temporal direction, and one without any fermion loop. The latter corresponds to the bosonic sector with fermion number $F = 0$ and the former to the fermionic sector with $F = 1$. This separation into the canonical sectors with fixed fermion number forms the basis for the solution of the fermion sign problem emerging in numerical Monte Carlo simulations of the quantum mechanical system with broken supersymmetry. For a detailed discussion of this issue we refer to the first paper in our series [1].

In the present paper we make use of the fact that in the bond formulation the weights of the bond configurations are completely localised and the local bond configuration states can be enumerated locally due to the discreteness of the new degrees of freedom. It is hence straightforward to construct a transfer matrix which in turn can be used to express the sum over all bond configurations, i.e., the partition function, as the trace over an appropriate product of the transfer matrix. As a consequence of the natural separation into bosonic and fermionic contributions the transfer matrix block diagonalises naturally into blocks with fixed fermion number, and this simplifies the calculations considerably. The transfer matrices do not depend on the imaginary time coordinate and hence contain all the physics of the system. It is therefore sufficient to understand the spectral properties of the transfer matrices and calculate physical observables such as the mass gaps directly from the eigenvalues of the transfer matrices. More complicated observables such as correlation functions and Ward identities can be calculated exactly using modified transfer matrices which include appropriate source terms.

As discussed above, the exact results at finite lattice spacing are most useful to gain a better understanding of the interplay between the various limits required in any lattice calculation, not restricted to supersymmetric quantum mechanics, in order to remove the infrared and ultraviolet regulators. In particular, we can study in detail how and under which circumstances supersymmetry is restored in the continuum and thermodynamic limit, and how, in the case of broken supersymmetry, the Goldstino mode emerges.

The outline of the paper is as follows. In Section 2, we derive explicitly the construction of the transfer matrices for supersymmetric quantum mechanics starting from the bond formulation of the lattice system. We then work out the calculation of various observables such as correlation functions in 2.2, the mass gaps from the eigenvalues of the transfer matrices in 2.3, and discuss some Ward identities which may be used to investigate the restoration of supersymmetry in the continuum in 2.4. After these technical considerations, we present our exact results in Section 3 for various observables of interest, such as the Witten index in 3.1 and correlation functions in 3.2. In addition, we demonstrate in detail how the supersymmetry is recovered in the continuum by means of energy spectra in 3.3 and Ward identities in 3.4, and finally present an exact calculation of the ground state energy in 3.5.

For each quantity we discuss in turn the results using the standard discretisation including the counterterm [2, 3] and the results for the Q -exact action [4]. We do so as far as possible for systems with unbroken and broken supersymmetry. Finally, in Section 4 we summarise our results and close with some conclusions, while in appendix A we provide some technical details concerning the numerical calculation of the transfer matrices.

2 The transfer matrix approach

In order to introduce the notation we briefly recall the Euclidean action for supersymmetric quantum mechanics involving the bosonic field ϕ and the fermionic fields $\bar{\psi}$ and ψ ,

$$S(\phi, \bar{\psi}, \psi) = \int_0^\beta dt \left\{ \frac{1}{2} \left(\frac{d\phi(t)}{dt} \right)^2 + \frac{1}{2} P'(\phi(t))^2 + \bar{\psi}(t) (\partial_t + P''(\phi(t))) \psi(t) \right\}. \quad (1)$$

The action depends on the superpotential $P(\phi)$ and is invariant under the two supersymmetry transformations

$$\begin{aligned} \delta_1 \phi &= \bar{\epsilon} \psi, & \delta_2 \phi &= \bar{\psi} \epsilon, \\ \delta_1 \psi &= 0, & \delta_2 \psi &= (\dot{\phi} - P') \epsilon, \\ \delta_1 \bar{\psi} &= -\bar{\epsilon} (\dot{\phi} + P'), & \delta_2 \bar{\psi} &= 0. \end{aligned} \quad (2)$$

Throughout our series of papers we use the superpotential

$$P_u(\phi) = \frac{1}{2} \mu \phi^2 + \frac{1}{4} g \phi^4 \quad (3)$$

as an example for unbroken supersymmetry with an additional parity symmetry $\phi \rightarrow -\phi$ and

$$P_b(\phi) = -\frac{\mu^2}{4\lambda} \phi + \frac{1}{3} \lambda \phi^3 \quad (4)$$

for broken supersymmetry with an additional combined parity and charge conjugation symmetry $\phi \rightarrow -\phi, \psi \rightarrow \bar{\psi}, \bar{\psi} \rightarrow \psi$.

After choosing a suitable discretisation of the derivatives, supersymmetric quantum mechanics can be formulated on the lattice in terms of bosonic and fermionic bond occupation numbers $n_i^b(x) \in \mathbb{N}_0$ and $n_i^f(x) = 0, 1$, respectively, connecting sites x and $x + 1$. We refer to our first paper [1] for further details and explanations. In particular, the partition function can be written as a sum over all allowed, possibly constrained, bond configurations $\mathcal{C} = \{n_i^b(x), n_i^f(x)\}$ in the configuration space \mathcal{Z} ,

$$Z = \sum_{\mathcal{C} \in \mathcal{Z}} W_F(\mathcal{C}) \quad (5)$$

where the weight $W_F(\mathcal{C})$ of a configuration is given by

$$W_F(\mathcal{C}) = \prod_x \left(\prod_i \frac{w_i^{n_i^b(x)}}{n_i^b(x)!} \right) \prod_x Q_F(N(x)). \quad (6)$$

Here, w_i is the weight of a bosonic bond b_i with $i \in \{j \rightarrow k \mid j, k \in \mathbb{N}\}$, while $F = 0, 1$ is the fermion number determined by the fermionic bond configuration $\{n^f(x)\}$. The site weight Q_F is given by

$$Q_F(N(x)) = \int_{-\infty}^{\infty} d\phi \phi^N(x) e^{-V(\phi)} M(\phi)^{1-F} \quad (7)$$

where

$$N(x) = \sum_{j,k} \left(j \cdot n_{j \rightarrow k}^b(x) + k \cdot n_{j \rightarrow k}^b(x-1) \right) \quad (8)$$

is the site occupation number, i.e., the total number of bosonic bonds connected to site x . Finally, the potential $V(\phi)$ and the monomer term $M(\phi)$ in eq.(7) depend on the superpotential $P(\phi)$ and the specifics of the chosen discretisation.

2.1 Transfer matrices and partition functions

We now express the bond formulation of supersymmetric quantum mechanics on the lattice in terms of transfer matrices. For the construction we start by considering a bond configuration \mathcal{C} in the configuration space \mathcal{Z} contributing to the partition function Z . The degrees of freedom are now expressed by means of bond occupation numbers $\{n_i^b(x), n^f(x)\}$ for the bosonic and fermionic bonds. These bonds connect nearest neighbouring lattice sites and it is hence natural to define bond states associated with the bonds of the lattice. The states are characterised by the fermionic and bosonic bond occupation numbers and are hence written as $|n^f(x), \{n_i^b(x)\}\rangle$, where the coordinate x refers to the bond connecting the sites x and $x+1$. The transfer matrix $T(x)$ then describes the transition of the bond state at $x-1$ to the bond state at x . Since the fermionic occupation number n^f , and hence the fermion number F , is conserved at each site, the transfer matrix decomposes into block diagonal form, each block representing separately the bosonic and fermionic sector. So the separation of bond configurations into the bosonic and fermionic sectors \mathcal{Z}_0 and \mathcal{Z}_1 , respectively, reflects itself in the block structure of the transfer matrix, and from now on it is sufficient to discuss separately the submatrices $T^F(x)$ with fixed fermionic bond occupation number $n^f = F$.

In figure 1 we give two examples for the characterisation of the transfer matrix for a system with only one type of bosonic bond $b_{1 \rightarrow 1}$ with corresponding occupation numbers $n_{1 \rightarrow 1}^b$ (dashed lines) in each of the sectors $F = 0, 1$. The occupation of the fermionic bond is

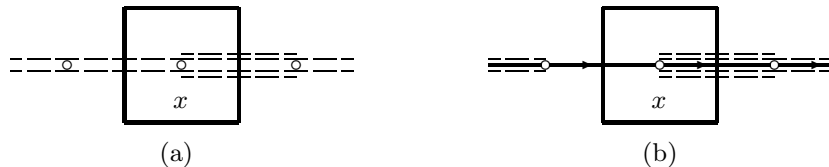


Figure 1: Graphical representation of the transfer matrix for a system with only one type of bosonic bond $b_{1 \rightarrow 1}$ with occupation numbers $n_{1 \rightarrow 1}^b$ (dashed lines). Plot (a) represents the entry $T_{2,4}^0$ of the transfer matrix in the bosonic sector and plot (b) shows the entry $T_{0,4}^1$ of the transfer matrix in the fermionic sector. The occupation of the fermionic bond is represented by the directed full line.

represented by the directed full line, cf. the first paper of our series [1] for further explanations on the graphical notation. In fact, since the characterisation of the set of states is independent of the coordinate x , it is sufficient to characterise the states just by $|n^f, \{n_i^b\}\rangle$ and hence the transfer matrix does not depend on x . As a consequence, the complete system for fixed

fermion number F is characterised by just one transfer matrix and all the physical information on the system can be extracted from it. This is a rather remarkable property of the bond formulation and stems from the fact that the reformulation of the continuous degrees of freedom into discrete ones allows a complete and explicit enumeration of all states. However, since there are no upper limits on the bosonic bond occupation numbers, the two matrices T^F , $F = 0, 1$ are infinitely large.

For a lattice consisting of L_t lattice points the partition function for both the fermionic and the bosonic sector can be calculated independently in terms of T^F as

$$Z_F = \text{Tr} \left[(T^F)^{L_t} \right] \quad (9)$$

where the transfer matrix multiplications now sum over all possible bond configurations and the matching of the bond configurations at the boundary is ensured by taking the trace. After diagonalisation of the transfer matrices one can calculate the partition functions equivalently via the eigenvalues λ_k^F of T^F ,

$$Z_F = \sum_k (\lambda_k^F)^{L_t}. \quad (10)$$

Eventually, the partition functions in the two sectors can then be combined as usual into partition functions with periodic and antiperiodic boundary conditions for the fermion as

$$Z_p = Z_0 - Z_1, \quad Z_a = Z_0 + Z_1. \quad (11)$$

Let us now write down the transfer matrix elements connecting the incoming state $|F, \{m_i^b\}\rangle$ with the outgoing state $|F, \{n_i^b\}\rangle$. This is straightforwardly done by comparing eq.(9) with eq.(5) and (6). Explicitly, we have

$$T_{\{m_i^b\}, \{n_i^b\}}^F = \sqrt{\prod_i \frac{w_i^{m_i^b} w_i^{n_i^b}}{m_i^b! n_i^b!}} Q_F(N) \quad (12)$$

where the site occupation number is given by $N = \sum_{j,k} (j \cdot n_{j \rightarrow k}^b + k \cdot m_{j \rightarrow k}^b)$. Here we choose to distribute the contributions $w^n/n!$ from the incoming and outgoing bonds symmetrically, but in principle one could choose any distribution, e.g. taking into account only contributions from the forward bonds.

To be more concrete, we now specify the general expression for the transfer matrices explicitly for the two discretisations discussed in detail in the first paper of our series [1] and for which we present exact results in this paper. The standard discretisation including the counterterm involves only one type of bosonic bond $b_{1 \rightarrow 1}$ carrying weight $w_{1 \rightarrow 1} = 1$ and the bond states can simply be labelled by the occupation number $n \equiv n_{1 \rightarrow 1}^b$. Explicitly, denoting the incoming state by $m \equiv m_{1 \rightarrow 1}^b$ and the outgoing by $n \equiv n_{1 \rightarrow 1}^b$ the transfer matrix can be written as

$$T_{m,n}^F = \sqrt{\frac{1}{m! \cdot n!}} Q_F(m+n). \quad (13)$$

For the Q -exact discretisation in addition to the bond $b_{1 \rightarrow 1}$ with weight $w_{1 \rightarrow 1}$ we have the new type of bond $b_{1 \rightarrow \nu}$ with weight $w_{1 \rightarrow \nu}$ where $\nu = 3$ for the superpotential P_u and $\nu = 2$ for the superpotential P_b . The explicit expressions for the weights are given in our first paper [1].

Labelling the incoming state by $m \equiv \{m_{1 \rightarrow 1}^b, m_{1 \rightarrow \nu}^b\}$ and the outgoing by $n \equiv \{n_{1 \rightarrow 1}^b, n_{1 \rightarrow \nu}^b\}$ we have

$$T_{m,n}^F = \sqrt{\frac{(w_{1 \rightarrow 1})^{m_{1 \rightarrow 1}^b + n_{1 \rightarrow 1}^b}}{(m_{1 \rightarrow 1}^b!)(n_{1 \rightarrow 1}^b!)}} \sqrt{\frac{(w_{1 \rightarrow \nu})^{m_{1 \rightarrow \nu}^b + n_{1 \rightarrow \nu}^b}}{(m_{1 \rightarrow \nu}^b!)(n_{1 \rightarrow \nu}^b!)}} Q_F(N) \quad (14)$$

where $N = n_{1 \rightarrow 1}^b + n_{1 \rightarrow \nu}^b + m_{1 \rightarrow 1}^b + \nu \cdot m_{1 \rightarrow \nu}^b$.

Note that depending on the additional symmetries present in the system, the bond configuration space may factorise further into sectors of fixed quantum numbers associated to the symmetries. This leads to an additional block structure in the transfer matrices T^F and it is then sufficient to discuss each of the submatrices separately. As an example we mention the \mathbb{Z}_2 parity symmetry present in the system with superpotential P_u in eq.(3). In that case the configuration space decomposes into configurations containing exclusively either even or odd bond occupation numbers. Consequently, this yields a decomposition of the transfer matrices into submatrices associated with the parity quantum numbers ± 1 .

Before discussing how various observables can be expressed in terms of the transfer matrices or their eigenvalues, we need to emphasise that one faces several numerical challenges when constructing and evaluating the transfer matrices. Firstly, as already mentioned, the matrices have infinite extent due to the fact that the bosonic bond occupation numbers are not limited and in practice one therefore needs to truncate the state space. Since the bond occupation numbers introduce a natural ordering of the states, it is straightforward to choose a cutoff such that the results are not affected. We discuss the technical aspects of this procedure in detail in appendix A.1. Secondly, the evaluation of the site weights tends to become numerically unstable for large values of the site occupation number. We will deal with this numerical problem in detail in the third paper of our series [5]. Thirdly, the numerical calculation of the transfer matrix elements can be rather delicate if the bond occupation numbers involved become large. We discuss strategies for a numerically stable determination of the transfer matrix elements in appendix A.2.

2.2 Correlation functions

Next, we extend the concept of transfer matrices to the calculation of correlation functions. Recalling from our first paper how the two-point functions are calculated in the bond language, we realise that the transfer matrix approach provides a perfect tool for the exact calculation of the bosonic as well as the fermionic two-point function. We first consider the bosonic case. To get a contribution to the expectation value of $\langle \phi_{x_1}^j \phi_{x_2}^k \rangle$, we have to add additional bosonic field variables at the sites x_1 and x_2 . The transfer matrices at these sites experience a corresponding modification and the graphical representation of the modified transfer matrix with additional bosonic sources is shown in figure 2 where we use the symbol \circ for each additional source. The additional variables affect the weight of the configuration via the occupation number $N(x) \rightarrow N(x) + j \cdot \delta_{x,x_1} + k \cdot \delta_{x,x_2}$. Thus, we introduce modified transfer matrices which allow for additional bosonic sources by defining

$$T_{\{m_i^b\}, \{n_i^b\}}^F(p) \equiv T_{\{m_i^b\}, \{n_i^b\}}^F(\phi^p) = \sqrt{\prod_i \frac{w_i^{m_i^b}}{m_i^b!} \frac{w_i^{n_i^b}}{n_i^b!}} Q_F(N + p), \quad (15)$$



Figure 2: Graphical representation of the bosonic transfer matrix at a site with additional bosonic sources. Plot (a) represents the matrix element $T_{2,4}^0(1)$ and plot (b) the matrix element $T_{2,4}^0(2)$ of a site with one and two additional sources, respectively.

such that we can calculate the non-normalised expectation value of an arbitrary n -point correlation function by using the transfer matrices $T^F(p)$, i.e.,

$$\langle\langle \phi_{x_1}^{p_1} \dots \phi_{x_n}^{p_n} \rangle\rangle_F = \text{Tr} \left[\prod_x T^F \left(\sum_{i=1}^n p_i \cdot \delta_{x, x_i} \right) \right]. \quad (16)$$

The originally defined transfer matrices in eq.(12) correspond to transfer matrices with no additional sources, $T^F(0) \equiv T^F$.

As a concrete example we now specify the non-normalised bosonic two-point correlation function $g_F^b(x_2 - x_1) = \langle\langle \phi_{x_1} \phi_{x_2} \rangle\rangle_F$. Defining $t = (x_2 - x_1) \bmod L_t$ and using translational invariance it reads

$$g_F^b(t) = \begin{cases} \text{Tr} \left[T^F(1) (T^F(0))^{t-1} T^F(1) (T^F(0))^{L_t-t-1} \right] & \text{if } t \neq 0, \\ \text{Tr} \left[T^F(2) (T^F(0))^{L_t-1} \right] & \text{if } t = 0. \end{cases} \quad (17)$$

For the connected part of the bosonic correlation function we also need the expectation value of ϕ . From the previous considerations it is easy to see that the non-normalised expectation value for any moment of ϕ can be calculated as

$$\langle\langle \phi^p \rangle\rangle_F = \text{Tr} \left[T^F(p) (T^F(0))^{L_t-1} \right]. \quad (18)$$

Eventually, the connected part of the bosonic correlation function for each sector is given by

$$C_{0,1}^b(t) = \frac{g_{0,1}^b(t)}{Z_{0,1}} - \left(\frac{\langle\langle \phi \rangle\rangle_{0,1}}{Z_{0,1}} \right)^2, \quad (19)$$

while for periodic and antiperiodic boundary conditions it is calculated according to the discussion in our first paper [1], i.e.,

$$C_p^b(t) = \frac{g_0^b(t) - g_1^b(t)}{Z_0 - Z_1} - \left(\frac{\langle\langle \phi \rangle\rangle_0 - \langle\langle \phi \rangle\rangle_1}{Z_0 - Z_1} \right)^2, \quad (20)$$

$$C_a^b(t) = \frac{g_0^b(t) + g_1^b(t)}{Z_0 + Z_1} - \left(\frac{\langle\langle \phi \rangle\rangle_0 + \langle\langle \phi \rangle\rangle_1}{Z_0 + Z_1} \right)^2 \quad (21)$$

for periodic and antiperiodic boundary conditions, respectively.

To construct the fermionic correlation function in the transfer matrix approach, we need to recall the structure of a bond configuration contributing to the fermionic two-point function from our first paper. In analogy to the bosonic case, we introduce new transfer matrices which

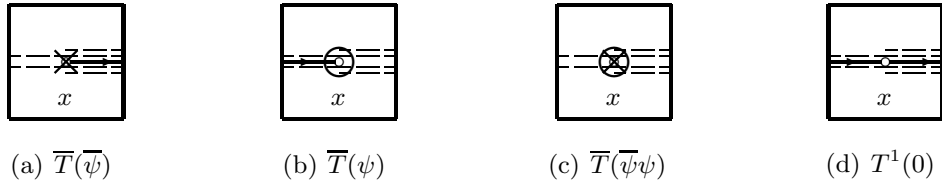


Figure 3: Graphical representation of the transfer matrices with additional fermionic sources. We use the symbol \times for the fermionic source $\overline{\psi}$ and \circ for the fermionic sink ψ . All examples are for the matrix element $\overline{T}_{2,4}$. The weights for the matrix elements (a)–(c) are the same and equal to the weight of (d).

take into account the additional fields $\overline{\psi}$ and ψ . In particular, we define a transfer matrix representing a site with a fermionic source and sink $\overline{T}(\overline{\psi}\psi)$, one representing a site with a fermionic source, $\overline{T}(\overline{\psi})$, and one with a fermionic sink, $\overline{T}(\psi)$. As usual, single additional fermionic variables have to be paired with a fermionic bond, an outgoing one to the right for a site with a source variable $\overline{\psi}$ and an incoming one from the left for a site with a sink variable ψ . The graphical representation for these transfer matrices is shown in figure 3 where we denote the fermionic source $\overline{\psi}$ by a bold \times and the fermionic sink ψ by a bold \circ . Using again $t = (x_1 - x_2) \bmod L_t$ the non-normalised fermionic correlation function $g^f(x_1 - x_2) = \langle\langle \psi_{x_1} \overline{\psi}_{x_2} \rangle\rangle$ can be composed of these matrices by

$$g^f(t) = \begin{cases} \text{Tr} \left[\overline{T}(\overline{\psi}) (T^1(0))^{t-1} \overline{T}(\psi) (T^0(0))^{L_t-t-1} \right] & \text{if } t \neq 0, \\ \text{Tr} \left[\overline{T}(\overline{\psi}\psi) (T^0(0))^{L_t-1} \right] & \text{if } t = 0. \end{cases} \quad (22)$$

Of course this expression can easily be generalised to take into account more complicated fermionic operators such as $\psi\phi^p$ and $\overline{\psi}\phi^p$. The additional presence of the bosonic variable ϕ^p simply increases the site occupation number according to the discussion on the bosonic correlation functions.

Since the weight of a site saturated with an additional fermionic source or sink paired with a fermionic bond is the same as the weight of a site saturated with two fermionic bonds or a source and a sink variable, the newly introduced transfer matrices all have the same entries as the transfer matrix $T^1(0)$, i.e.,

$$\overline{T}(\overline{\psi}) = \overline{T}(\psi) = \overline{T}(\overline{\psi}\psi) = T^1(0). \quad (23)$$

Therefore, the definition of new matrices for sites with additional fermionic variables is in fact obsolete in practice and the presence of a fermionic source or sink expresses itself by a change from T^0 to T^1 and vice versa. The non-normalised fermionic two-point function can hence be written in terms of the matrices $T^1(0)$ and $T^0(0)$ as

$$g^f(t) = \text{Tr} \left[(T^1(0))^{t+1} (T^0(0))^{L_t-t-1} \right]. \quad (24)$$

Yet, the formation of the fermionic correlation function is a little more subtle than the one of the bosonic correlation function. The translation invariance of the two-point function together with the cyclic invariance of the trace amounts to the fact that $g^f(t)$ is a superposition of *all possible* configurations with an open fermionic string where the fermionic source and the sink are separated by the distance t . For a given bosonic bond configuration, there are thus L_t different configurations with an open fermionic string. For t of them, the fermionic

string crosses the boundary and for antiperiodic boundary conditions, we have to account for those as they pick up a negative sign. Keeping track of all the signs correctly, the fermionic correlation functions for periodic and antiperiodic boundary conditions, respectively, read

$$C_p^f(t) = \frac{g^f(t)}{Z_0 - Z_1}, \quad C_a^f(t) = \frac{L_t - 2t}{L_t} \frac{g^f(t)}{Z_0 + Z_1}. \quad (25)$$

From our discussion of the fermionic two-point function in our first paper [1] we remember that it is really only defined in the bosonic sector $F = 0$ and we have

$$C_0^f = \frac{g^f(t)}{Z_0}. \quad (26)$$

On the other hand, we can interpret the open fermion string of length t as an open antifermion string of complementary length $L_t - t$ on the background of bond configurations in sector $F = 1$. This interpretation becomes evident when one calculates the energy or mass gaps from the correlation functions in terms of the eigenvalues of the transfer matrices which we are going to do in the next section.

2.3 Mass gaps

Observables closely related to the correlation functions are of course the energy or mass gaps. It is well known that in the transfer matrix formalism these mass gaps can be calculated directly from the ratios of eigenvalues of the transfer matrices, cf. [6] for the explicit calculation in our supersymmetric quantum mechanics setup. Ordering the eigenvalues of the transfer matrix T^F according to

$$\lambda_0^F > \lambda_1^F > \dots, \quad (27)$$

the calculation of the i -th fermionic mass gap in the bosonic sector yields

$$m_i^f = -\ln(\lambda_i^1/\lambda_0^0). \quad (28)$$

By interpreting the expectation value $\langle \bar{\psi}_t \psi_0 \rangle = C^{\bar{f}}(t)$ as the correlator of the antifermion \bar{f} in the fermionic sector $F = 1$, we can similarly calculate its mass via

$$m_i^{\bar{f}} = -\ln(\lambda_i^0/\lambda_0^1), \quad (29)$$

and we see that the masses of the fermion and antifermion are the same – at least in the continuum – up to a minus sign. Of course, this is in accordance with the standard quantum mechanical interpretation of an antiparticle as a particle with negative energy propagating backward in time, and so this confirms our interpretation of the open fermion string as a propagating fermion in sector $F = 0$ or as a complementary antifermion in sector $F = 1$. The bosonic mass gaps are defined in each sector $F = 0, 1$ individually and are calculated as

$$m_{i,F}^b = -\ln(\lambda_i^F/\lambda_0^F). \quad (30)$$

It is useful to illustrate schematically which mass gap is measured with respect to which vacuum via the ratios of the eigenvalues. In figures 4 and 5 the mass gaps in the bosonic sector, i.e., with respect to the bosonic vacuum, are depicted by full lines while the mass gaps

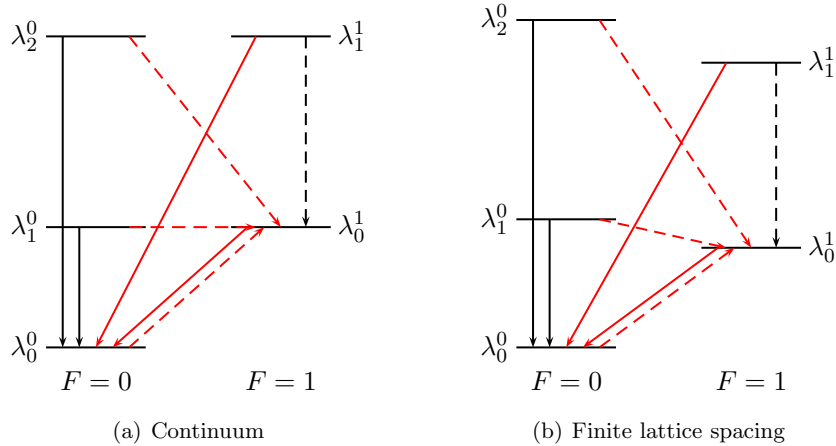


Figure 4: Unbroken supersymmetric quantum mechanics. The energy levels and the respective mass gaps in the continuum (a), and for finite lattice spacing (b) where the energy levels are shifted w.r.t. to the ones in the continuum due to discretisation artefacts.

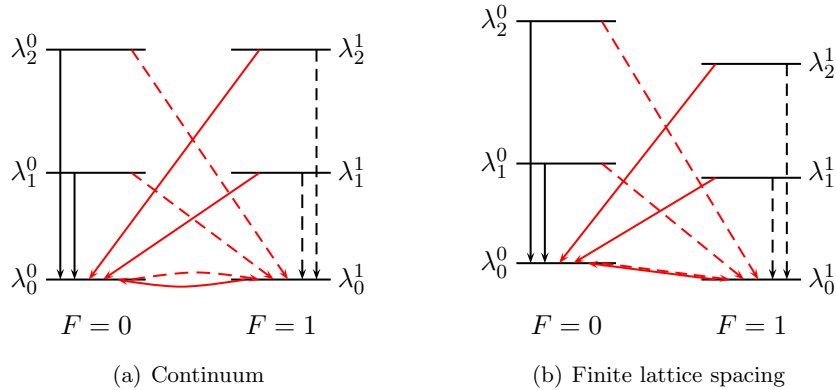


Figure 5: Broken supersymmetric quantum mechanics. The energy levels and the respective mass gaps in the continuum (a), and for finite lattice spacing (b) where the energy levels are shifted w.r.t. to the ones in the continuum due to discretisation artefacts. Note that the plot (b) illustrates a situation in which the fermionic vacuum is favoured at finite lattice spacing as compared to the bosonic vacuum.

in the fermionic sector, i.e., with respect to the fermionic vacuum, are drawn as dashed lines. Bosonic mass gaps $m_{i,F}^b$ with bosonic quantum numbers are further differentiated from the fermionic mass gaps $m_{i,\bar{F}}^f$ with fermionic quantum numbers as black versus red lines. Figure 4 illustrates a system with unbroken supersymmetry and a unique bosonic ground state in the continuum (a) and at finite lattice spacing (b), while figure 5 illustrates a system with broken supersymmetry and hence two degenerate bosonic and fermionic ground states, again in the continuum (a) and at finite lattice spacing (b). The shifts in the energy levels w.r.t. to the ones in the continuum are due to discretisation artefacts of $\mathcal{O}(a)$ and are expected to disappear in the continuum. Illustration (b) in figure 5 represents a situation in which the fermionic vacuum is favoured at finite lattice spacing as compared to the bosonic vacuum. Moreover, it is interesting to note that unless the vacua are degenerate, there is always one negative fermionic mass gap, namely the one measured from the energetically lower to the higher vacuum.

2.4 Ward identities

One of the main goals of our efforts in supersymmetric quantum mechanics is to gain a precise understanding of whether and how supersymmetry is restored in the continuum limit. For such investigations Ward identities are most useful and many of our exact results discussed in this paper refer to various Ward identities which can be derived for the different discretisations we consider. A Ward identity can be derived by rewriting the expectation value of an observable $\mathcal{O}(\phi)$ in the path integral formulation for the transformed variable, $\phi \rightarrow \phi' = \phi + \delta\phi$, assuming that the measure of the path integral is invariant under this variation, $\mathcal{D}\phi' = \mathcal{D}\phi$. Since the physics cannot depend on the shift of the integration variable, we find to leading order in δ

$$\begin{aligned}\langle \mathcal{O} \rangle &= \frac{1}{Z} \int \mathcal{D}\phi' \mathcal{O}(\phi') e^{-S(\phi')} \\ &= \frac{1}{Z} \int \mathcal{D}\phi (\mathcal{O}(\phi) + \delta\mathcal{O}(\phi)) e^{-S(\phi)} (1 - \delta S(\phi)) \\ &= \langle \mathcal{O} \rangle + \langle \delta\mathcal{O} \rangle - \langle \mathcal{O}\delta S \rangle,\end{aligned}$$

and therefore the relation

$$\langle \delta\mathcal{O} \rangle = \langle \mathcal{O}\delta S \rangle \quad (31)$$

must hold for any observable. Now, if the action is invariant under the transformation δ , the r.h.s. of the equation vanishes, yielding

$$\langle \delta\mathcal{O} \rangle = 0 \quad (32)$$

as a condition to test whether the symmetry is indeed restored in the continuum.

As a first example, we consider the observable $\mathcal{O} = \bar{\psi}$. Its variation under the lattice version of the supersymmetry transformation δ_1 in eq.(2) results in the simple Ward identity

$$W_0 \equiv \langle (\nabla^- \phi + P') \rangle = 0. \quad (33)$$

Thus, the vanishing of the expectation value of the first derivative of the superpotential $\langle P' \rangle$ in the continuum indicates restoration of supersymmetry. Note that the variation of the operator $\mathcal{O} = \bar{\psi}$ under the supersymmetry transformation δ_2 yields $\delta_2 \bar{\psi} = 0$ by definition.

As a second example we consider the observable $\mathcal{O} = \bar{\psi}_x \phi_y$. Its variation under the supersymmetry transformation δ_1 yields Ward identities which connect bosonic and fermionic correlation functions. In particular, we obtain

$$W_1(y-x) \equiv \langle \bar{\psi}_x \psi_y \rangle + \langle (\nabla^- \phi + P')_x \phi_y \rangle = 0, \quad (34)$$

while the variation of the operator under the supersymmetry transformation δ_2 vanishes trivially. Analogously, one can use the observable $\mathcal{O} = \psi_x \phi_y$ which under the supersymmetry transformation δ_2 yields a similar set of Ward identities,

$$W_2(x-y) \equiv \langle \psi_x \bar{\psi}_y \rangle + \langle (\nabla^- \phi - P')_x \phi_y \rangle = 0, \quad (35)$$

while the variation of the operator under the other supersymmetry transformation δ_1 vanishes trivially.

Let us now be more specific and calculate the Ward identities W_0, W_1 and W_2 explicitly for the two superpotentials P_u and P_b employed in our investigation. Using the translational invariance of the lattice, for the superpotential P_u we find the Ward identities

$$W_0 = \langle P'_u \rangle = \mu \langle \phi \rangle + g \langle \phi^3 \rangle, \quad (36)$$

$$W_1(t) = -\langle \psi_t \bar{\psi}_0 \rangle + (1 + \mu) \langle \phi_t \phi_0 \rangle - \langle \phi_{t+1} \phi_0 \rangle + g \langle \phi_t \phi_0^3 \rangle, \quad (37)$$

$$W_2(t) = \langle \psi_t \bar{\psi}_0 \rangle + (1 - \mu) \langle \phi_t \phi_0 \rangle - \langle \phi_{t+1} \phi_0 \rangle - g \langle \phi_t^3 \phi_0 \rangle, \quad (38)$$

while for the superpotential P_b , we obtain analogously

$$W_0 = \langle P'_b \rangle = -\frac{\mu^2}{4\lambda} + \lambda \langle \phi^2 \rangle, \quad (39)$$

$$W_1(t) = -\langle \psi_t \bar{\psi}_0 \rangle + \langle \phi_t \phi_0 \rangle - \langle \phi_{t+1} \phi_0 \rangle - \frac{\mu^2}{4\lambda} \langle \phi \rangle + \lambda \langle \phi_t \phi_0^2 \rangle, \quad (40)$$

$$W_2(t) = \langle \psi_t \bar{\psi}_0 \rangle + \langle \phi_t \phi_0 \rangle - \langle \phi_{t+1} \phi_0 \rangle + \frac{\mu^2}{4\lambda} \langle \phi \rangle - \lambda \langle \phi_t^2 \phi_0 \rangle. \quad (41)$$

With this we conclude the discussion of the observables which we investigate in the following, and we now proceed to the discussion of the results.

3 Exact results

In this section, we present our exact lattice results for the action with counterterm as well as for the Q -exact action by employing the transfer matrix technique. For the two superpotentials P_u and P_b , the actions are given explicitly in the first paper of our series [1]. For our further discussion it is useful to recall that the continuum limit is taken by fixing the dimensionful parameters μ, g, λ and L while taking the lattice spacing $a \rightarrow 0$. In practice, the dimensionless ratios $f_u = g/\mu^2, f_b = \lambda/\mu^{3/2}$ fix the couplings and μL the extent of the system in units of μ , while $a\mu$ and a/L are subsequently sent to zero. We perform our calculations for couplings f_u and f_g which lie well outside of the perturbative regime in order to assess the systematics of the nonperturbative lattice calculations. Finally, we also recall that for antiperiodic fermionic boundary conditions the finite extent μL corresponds to finite inverse temperature in units of μ and the limit $\mu L \rightarrow \infty$ is therefore required to recover the system at zero temperature.

3.1 The ratio Z_p/Z_a and the Witten index W

We start by calculating the ratio Z_p/Z_a . At zero temperature this ratio is equal to the Witten index and represents therefore an important indicator for whether supersymmetry is broken or not. In quantum mechanics, whether or not supersymmetry is broken is not a dynamical question, but depends solely on the asymptotic form of the superpotential. For unbroken supersymmetry, the bosonic vacuum lies well below the fermionic one (or vice versa). Thus, in the zero temperature limit $\mu L \rightarrow \infty$ only the bosonic sector contributes to the partition function while the fermionic contribution Z_1 vanishes, such that

$$W = \lim_{\mu L \rightarrow \infty} \frac{Z_p}{Z_a} = \lim_{\mu L \rightarrow \infty} \frac{Z_0 - Z_1}{Z_0 + Z_1} \longrightarrow 1. \quad (42)$$

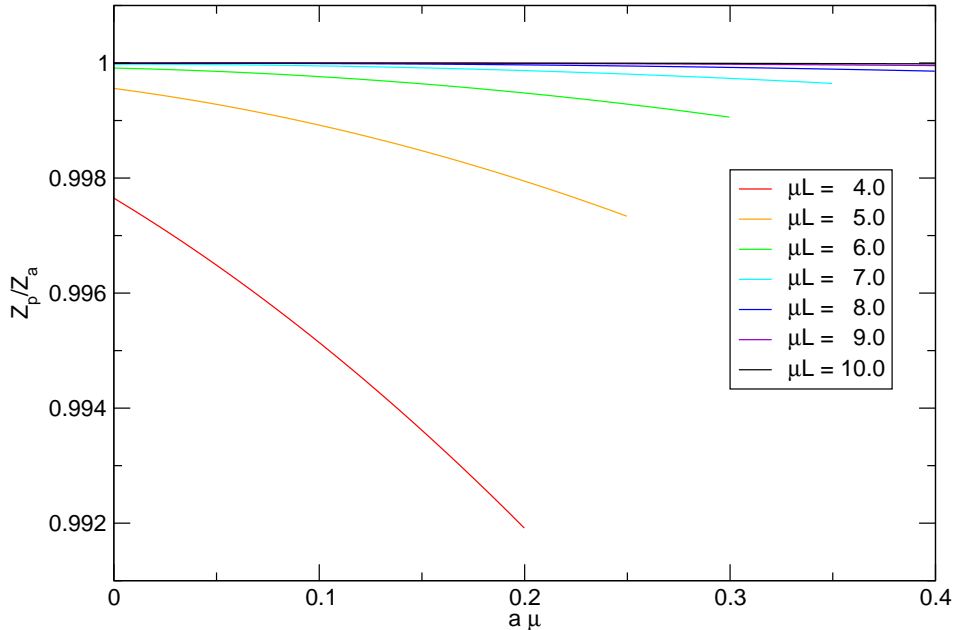


Figure 6: Unbroken supersymmetric quantum mechanics, standard discretisation. Continuum extrapolation of the ratio Z_p/Z_a for different values of μL at fixed coupling $f_u = 1$.

For finite extent μL (nonzero temperature), there are nonvanishing contributions from the fermionic vacuum, i.e., the partition function Z_1 is no longer zero due to quantum (thermal) fluctuations, resulting in a ratio $Z_p/Z_a < 1$. To leading order in the inverse temperature, the asymptotic dependence is governed by the energy gap m_0^f between the fermionic and bosonic vacuum,

$$\frac{Z_p}{Z_a} \sim \frac{1}{1 + 2e^{-m_0^f L}}. \quad (43)$$

For broken supersymmetry on the other hand, both vacua are equally preferable in the continuum and all bosonic and fermionic energy levels are degenerate. Therefore we have $Z_0 = Z_1$ and the Witten index goes to zero,

$$W = \frac{Z_p}{Z_a} = \frac{Z_0 - Z_1}{Z_0 + Z_1} \rightarrow 0 \quad (44)$$

independent of the extent or temperature of the system. Using our exact lattice calculation we can now investigate how these continuum expectations are modified at finite lattice spacing and how the continuum limit is eventually realised.

First, we consider unbroken supersymmetry. In figure 6, we plot the ratio Z_p/Z_a versus $a\mu$ for different values of fixed μL using the standard discretisation for fixed coupling $f_u = 1$. At nonzero temperature we observe leading order lattice artefacts which are linear in a . In the zero temperature limit they are suppressed and the leading artefacts eventually become $\mathcal{O}(a^2)$. Moreover, the artefacts become very small in this limit, simply because at zero temperature only the bosonic groundstate contributes and the nondegeneracies of the excited states at finite a , cf. figure 4, become irrelevant. As the temperature increases, the system gets more sensitive to the excited states since their contributions to the partition function grow larger, and consequently the nondegeneracies between the bosonic and fermionic energy levels

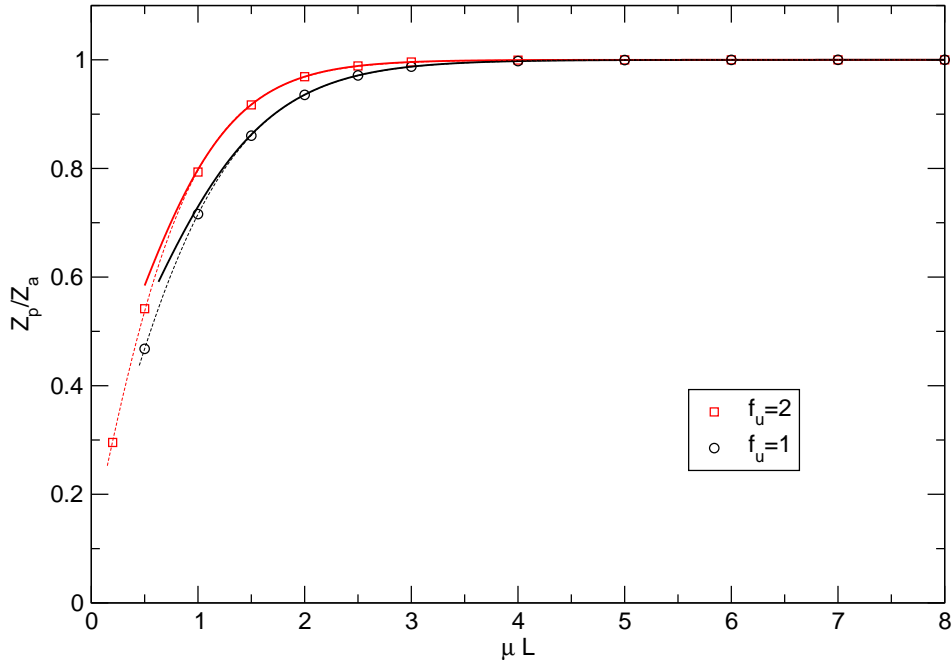


Figure 7: Unbroken supersymmetric quantum mechanics. The continuum values of the ratio Z_p/Z_a versus μL for different couplings $f_u = 1$ (black circles) and $f_u = 2$ (red squares). The full lines describe the asymptotic behaviour according to eq.(43) while the dashed lines include additional higher order contributions.

crystallise in the growing lattice artefacts. In the continuum limit, we observe the expected deviation of the ratio Z_p/Z_a from one as discussed above. In figure 7, we show the continuum value of the ratio Z_p/Z_a as a function of the inverse temperature μL for two different couplings $f_u = 1$ and $f_u = 2$. The full lines indicate the asymptotic behaviour for $\mu L \rightarrow \infty$ according to eq.(43), while the dashed lines include additional higher order contributions. It can be seen that the system reaches the asymptotic zero temperature behaviour already at moderate values of μL . Moreover, contributions from the fermionic vacuum to the partition function are essentially negligible for $\mu L \gtrsim 4$.

For broken supersymmetry we plot the continuum limit of the ratio Z_p/Z_a versus $a\mu$ for different values of μL at fixed coupling $f_b = 1$ using the standard discretisation in figure 8. First we note that the ratio goes to zero towards the continuum limit indicating a vanishing Witten index in that limit independent of the temperature. This is the expected continuum behaviour as argued above in eq.(44) and relies on the fact that the bosonic and fermionic energy levels become degenerate in pairs. Since the lattice discretisation breaks this degeneracy explicitly, cf. figure 5, the ratio is nonzero at finite lattice spacing. One can think of the finite lattice spacing as regulating the Goldstino zero mode and the energy difference between the two vacua simply corresponds to the regulated Goldstino mass. As a consequence the associated vanishing Witten index is regulated, too. As explained in detail in the first paper of our series [1] a vanishing Witten index leads to a fermion sign problem for Monte Carlo simulations. Since the finite lattice spacing regulates the index one could argue that the sign problem is avoided in this way, but of course it is not clear whether the lattice artefacts and the statistical fluctuations can be kept under control. In fact it turns out that the lattice artefacts for the ratio Z_p/Z_a can become extremely strong. While the leading artefacts

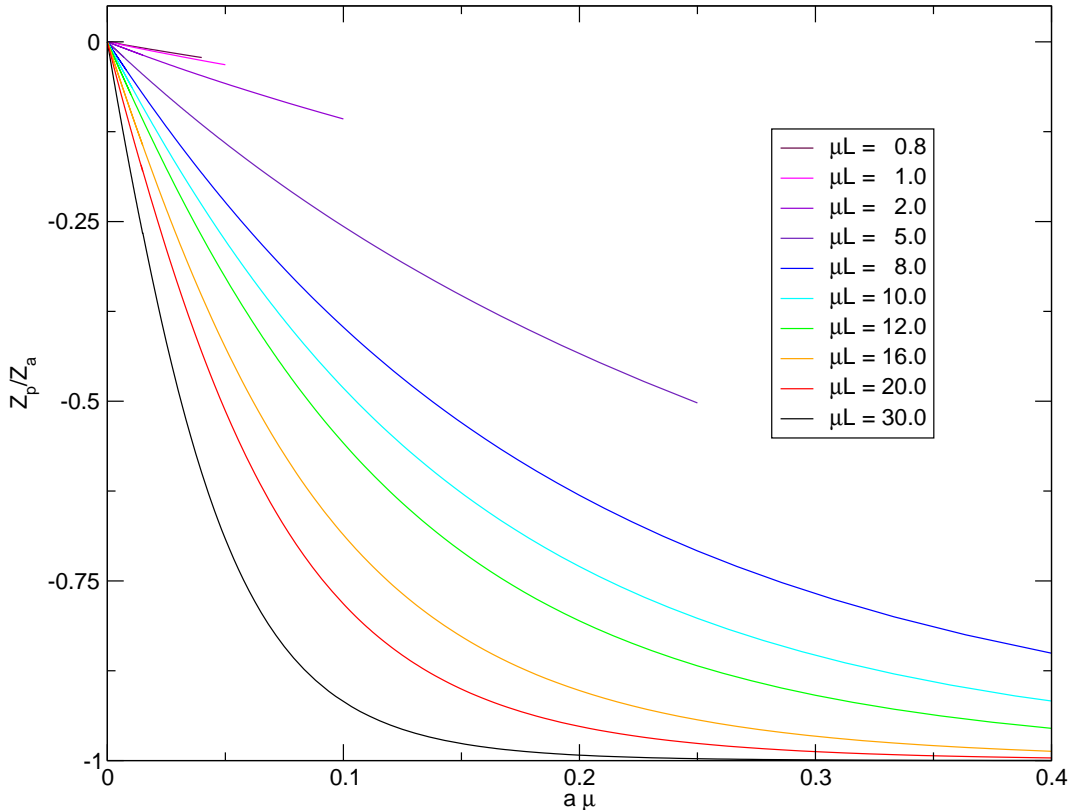


Figure 8: Broken supersymmetric quantum mechanics, standard discretisation. Continuum extrapolation of the ratio Z_p/Z_a for different values of μL at fixed coupling $f_b = 1$.

are evidently $\mathcal{O}(a)$, they grow exponentially large as the temperature is lowered, i.e., at low temperature artefacts of all orders in a become relevant such that the finite lattice spacing corrections in the ratio are exponentially enhanced towards low temperatures.

The rather peculiar behaviour of the lattice corrections for small temperatures can be explained as follows. Considering the illustration of the supersymmetry broken spectrum at finite a in figure 5, it is clear that the degeneracy between the bosonic and fermionic vacuum is lifted. For small temperatures (large values of μL) the tunnelling from the energetically lower to the higher vacuum are exponentially suppressed with growing μL . On the other hand, exactly these tunnellings are needed in order for the higher vacuum to contribute to the partition function, eventually leading to the vanishing Witten index. Only once the temperature is large enough compared to the energy difference between the two vacua, i.e. the regulated Goldstino mass, the tunnelling becomes effective enough to drive the Witten index to zero. Equivalently, at fixed temperature the Goldstino mass, which to leading order is proportional to $a\mu$, needs to become sufficiently small, and from figure 8 it becomes evident when this is the case.

The exponentially enhanced lattice artefacts have a rather dramatic consequence for the Witten index concerning the order of the limits $\mu L \rightarrow \infty$ and $a \rightarrow 0$. As is evident from our discussion and the data in figure 8, extrapolating the index to $\mu L \rightarrow \infty$ always yields $W = -1$ at *any* finite lattice spacing. Therefore the subsequent continuum limit of the index at zero temperature comes out incorrectly and the expectation in eq.(44) is hence not confirmed. So

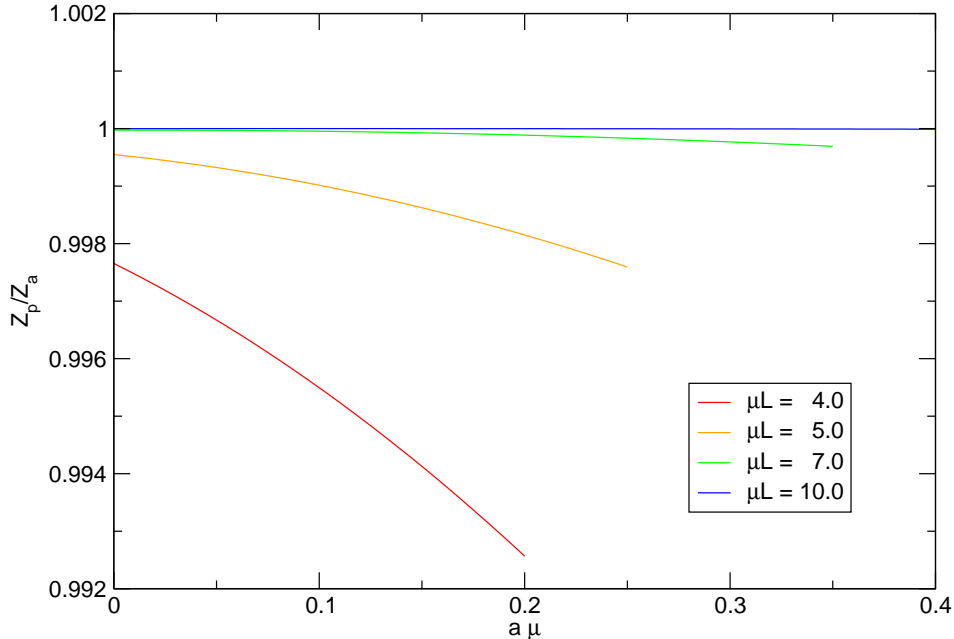


Figure 9: Unbroken supersymmetric quantum mechanics, Q -exact discretisation. Continuum extrapolation of the ratio Z_p/Z_a for different values of μL at fixed coupling $f_u = 1$.

in contrast to unbroken supersymmetry, here the order of the limits is crucial and has to be taken into account for the correct interpretation of the results. Finally, from the plot we infer that the fermionic vacuum has a lower energy than the bosonic one, hence the Witten index tends to -1 for finite lattice spacing, i.e., the picture at finite a is exactly as depicted in Fig. 5.

Next, we consider the results for the Witten index using the Q -exact discretisation. In figure 9 we plot the ratio Z_p/Z_a versus $a\mu$ for different values of μL at fixed coupling $f_u = 1$ for the case when supersymmetry is unbroken. We observe lattice artefacts which are almost identical to the ones found with the standard discretisation. In addition, in the continuum the ratios converge to the same values for any given inverse temperature μL and the temperature dependence in the continuum is therefore given exactly as in figure 7. Of course the agreement is a consequence of the universality of lattice calculations in the continuum which is nicely confirmed by our results. Turning to the case when supersymmetry is broken, the results for the Q -exact discretisation are rather boring. Since the degeneracy between the bosonic and fermionic energy levels is maintained exactly at any value of the lattice spacing a , the contributions from the bosonic and fermionic sector are always exactly equal and cancel precisely, hence the Witten index is zero independent of the temperature. Note however that the exact degeneracy of the energy levels does not exclude lattice artefacts in the spectrum. In fact, they are rather large as we will see in Section 3.3, but the Witten index is not sensitive to it as long as the degeneracy between the bosonic and fermionic levels is maintained at finite lattice spacing.

3.2 Correlation functions

In this section, we present some exact results for two-point correlation functions, merely as qualitative illustrations of how they are affected by lattice artefacts. A more quantitative discussion will follow in Section 3.3, where we consider the energy gaps, and in Section 3.4 where we investigate Ward identities relating fermionic and bosonic correlation functions.

First, we show the bosonic and the fermionic correlation function for unbroken supersymmetry using the standard discretisation. In figure 10(a) we display the bosonic and fermionic two-point correlation functions $C^{b,f}(t)$ for periodic and antiperiodic b.c., respectively, at fixed coupling $f_u = 1$ for $\mu L = 2$ corresponding to a high temperature. In figure 10(b) the same correlation functions are displayed for $\mu L = 10$ corresponding to a low temperature. For $\mu L = 2$, we know from Section 3.1 that finite temperature effects are not negligible. In figure 10(a) these effects are reflected by the fact that the correlation functions for periodic and antiperiodic b.c. are clearly distinguishable, i.e., they are sensitive to the boundary conditions. For $\mu L = 10$, we are in a regime where the system behaves as being close to zero temperature where the system is dominated by the bosonic vacuum. Thus, the bosonic correlation functions receive contributions only from the bosonic sector and are hence no longer distinguishable for periodic and antiperiodic b.c. as illustrated in figure 10(b). The fermionic correlation functions on the other hand are different for periodic and antiperiodic b.c. even for this choice of parameters. This difference originates from the specific implementation of the boundary conditions via eq.(25) which takes into account how many times an open fermion string of length t can cross the boundary when the translational invariance of the correlation function is incorporated. To complete our discussion for unbroken supersymmetry, in figure 11 we display the correlation functions for the same calculation as above, but individually for each sector F according to eq.(19) and (26). Note that we only plot the fermionic correlation function $C_0^f(t)$ in the bosonic sector $F = 0$, but not the antifermionic correlation function $C_1^{\bar{f}}(t)$ in the fermionic sector $F = 1$, cf. our discussion in [1] and above in Section 2.3 and 2.2. The bosonic correlation functions are shown in both the bosonic and fermionic sector. However, in this temperature regime $Z_0 \gg Z_1$ and therefore, the bosonic correlation function in the fermionic sector $C_1^b(t)$ is heavily suppressed with respect to the one in the bosonic sector $C_0^b(t)$ when contributing to the correlation function $C_{p,a}^b(t)$ with fixed fermionic boundary conditions. It is also interesting to note that the correlation functions consist of a single exponential term only, i.e., the overlap of the operators ϕ and ψ with the state corresponding to the lowest mass gap is maximal.

We now turn to the analogous correlation functions for broken supersymmetry. In figure 12, the bosonic and the fermionic correlation functions are displayed for periodic and antiperiodic b.c. for $\mu L = 10$ at fixed coupling $f_b = 1$. In contrast to unbroken supersymmetry, the bosonic correlation functions do not approach zero for $t/L \sim 1/2$. To get an understanding for this, we first need to consider figure 13 where we show the continuum extrapolation for $\langle \phi \rangle$ in the same physical situation, i.e. at $\mu L = 10$ and $f_b = 1$. For each sector the expectation value $\langle \phi \rangle_F$ extrapolates to the same value but with opposite sign. This is expected because of the additional \mathbb{Z}_2 -symmetry for the superpotential P_b . Furthermore, figure 8 suggests that both sectors Z_0 and Z_1 are weighted equally in the continuum. Therefore, on the one hand, $\langle \phi \rangle_a \rightarrow 0$. On the other hand, for periodic b.c., the numerator takes a fixed value while the denominator goes to zero and the expectation value $\langle \phi \rangle_p$ is thus ill-defined in the continuum¹.

¹Note, however, that for example $\langle \phi^2 \rangle_p$ is well defined in the continuum, cf. Section 3.4.

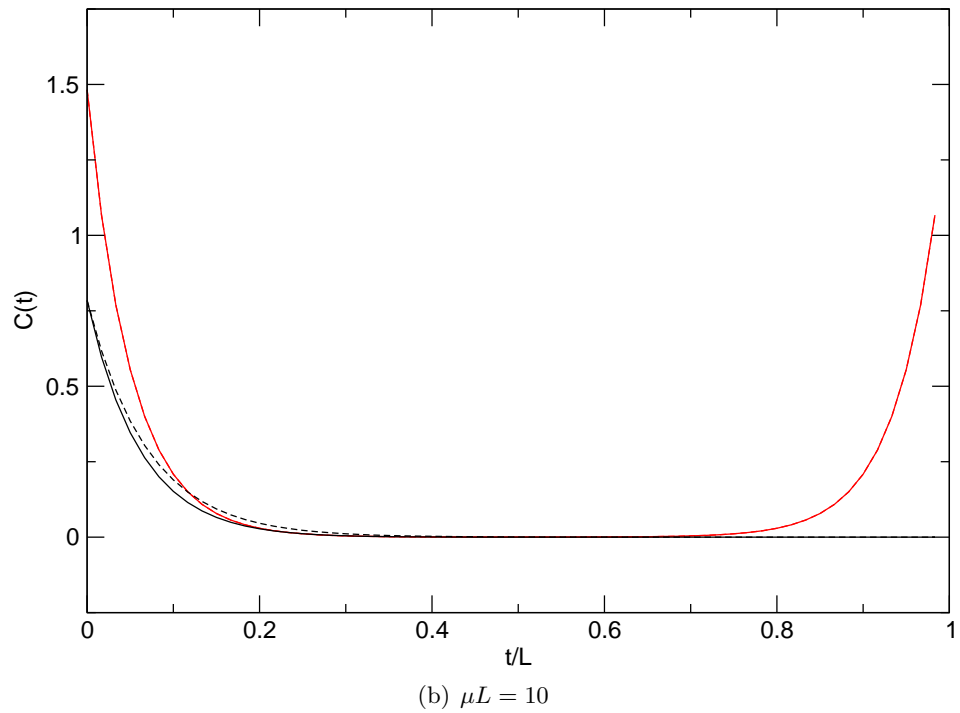
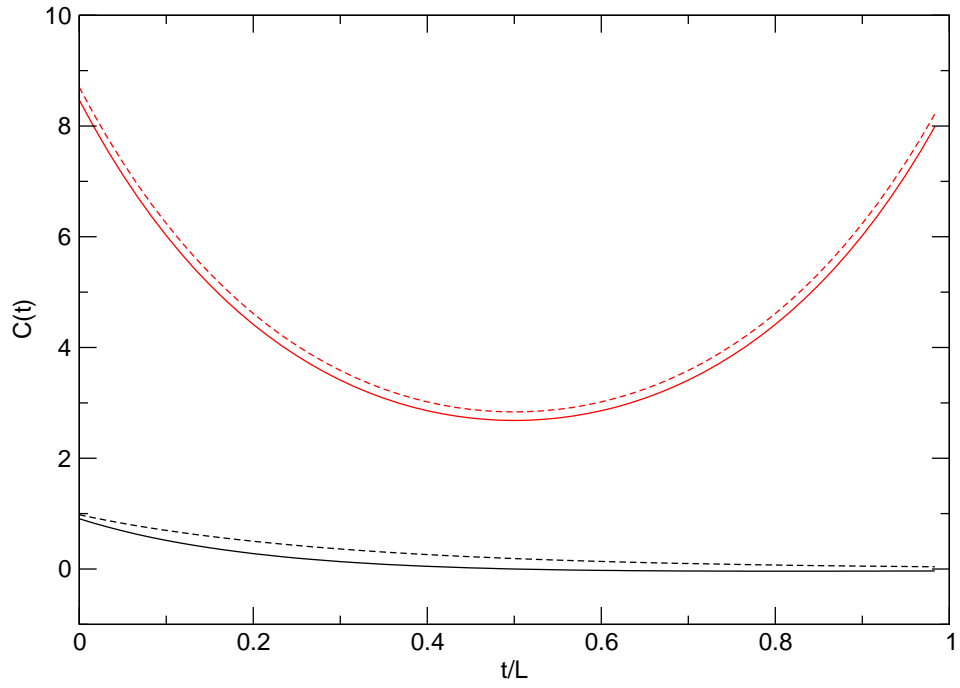


Figure 10: Unbroken supersymmetric quantum mechanics, standard discretisation. The bosonic (red) and fermionic (black) correlation functions for periodic (dashed) and antiperiodic boundary conditions (solid) at fixed coupling $f_u = 1$. Note that in plot (b) the bosonic correlation functions for periodic and antiperiodic b.c. are indistinguishable.

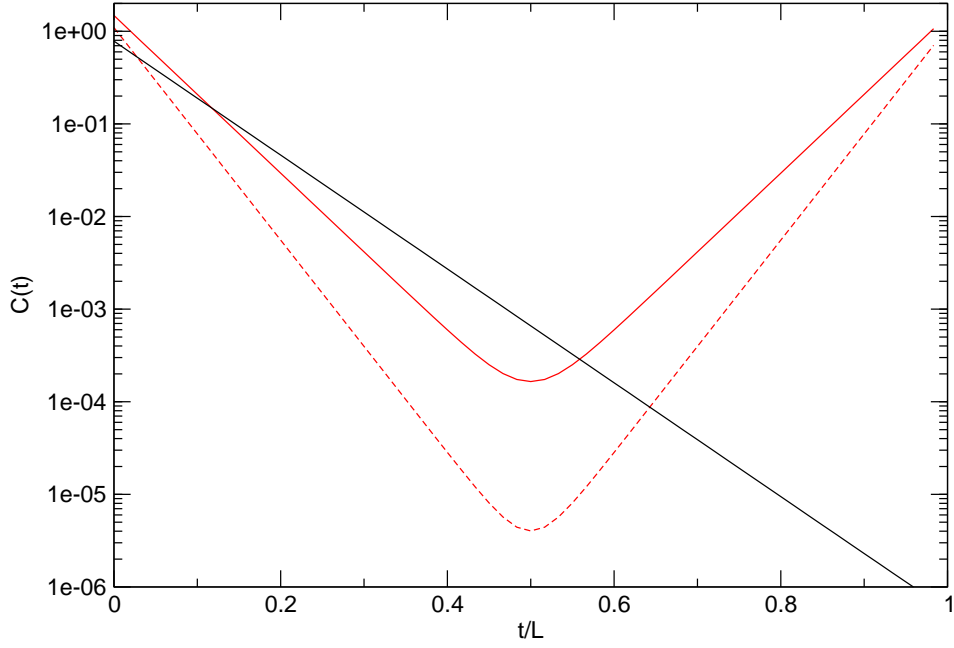


Figure 11: Unbroken supersymmetric quantum mechanics, standard discretisation. The bosonic (red) and fermionic (black) correlation functions in the bosonic sector $F = 0$ (solid) and the bosonic correlation function in the fermionic sector $F = 1$ (dashed) for $\mu L = 10$ and coupling $f_u = 1$.

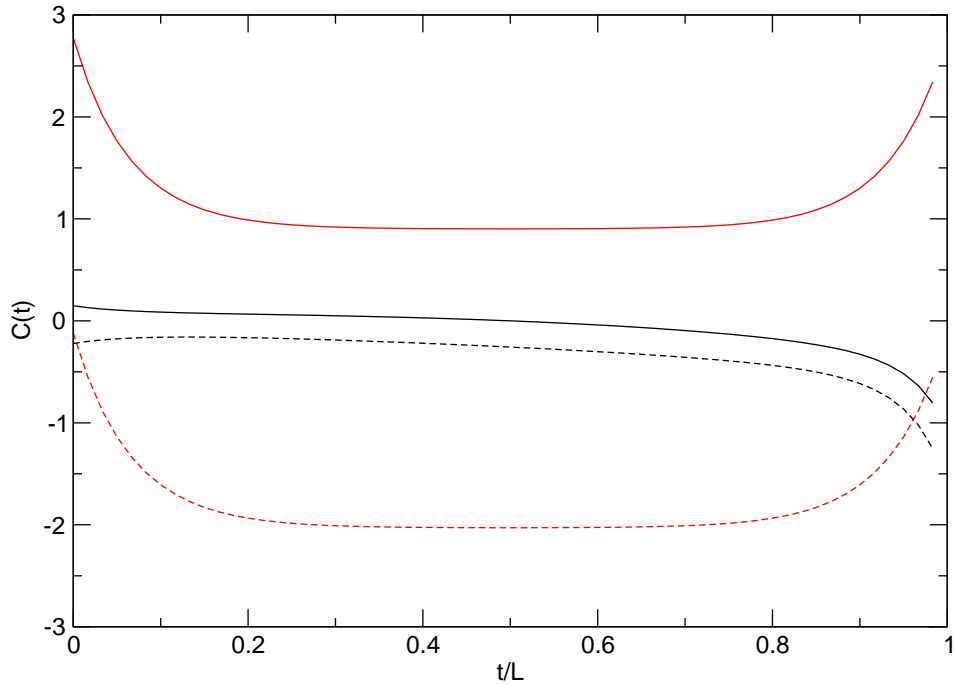


Figure 12: Broken supersymmetric quantum mechanics, standard discretisation. The bosonic (red) and fermionic (black) correlation functions for periodic (dashed) and antiperiodic b.c. (solid) for $\mu L = 10$ and coupling $f_b = 1$.

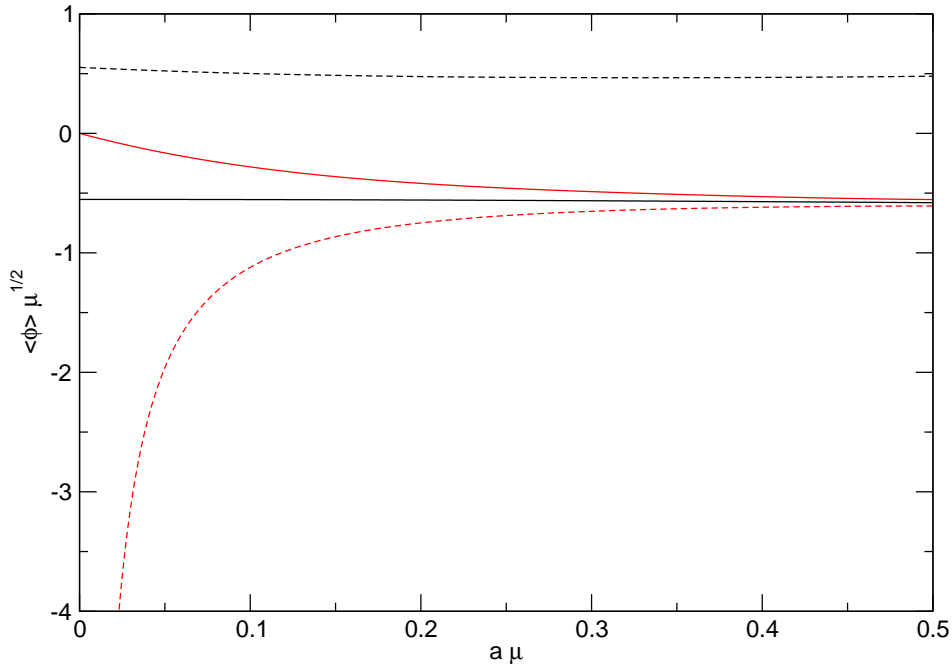


Figure 13: Broken supersymmetric quantum mechanics, standard discretisation. Continuum extrapolation of $\langle \phi \rangle$ in the sectors Z_0 (black dashed line) and Z_1 (black solid line), for antiperiodic (solid red line) and periodic boundary conditions (dashed red line) at $\mu L = 10$ and $f_b = 1$.

After these considerations concerning the expectation value of ϕ , we are now able to explain the rather strange fact that the bosonic correlation function has a negative offset. Instead of removing a possible constant offset in the connected bosonic two-point function, the term $\langle \phi \rangle_p^2$ shifts the correlation function to negative values. This problem of the shift into the negative worsens closer to the continuum because the term $-\langle \phi \rangle_p^2$ takes larger negative values for smaller lattice spacings. The bosonic correlation function is therefore an ill-defined observable in the continuum for periodic boundary conditions. It is therefore necessary to look at the correlation function in each sector individually and we do so in figure 14. We observe that the bosonic correlation functions are very similar in each sector. Note, that the term $\langle \phi \rangle_F^2$ for the correlation functions measured independently in the bosonic and fermionic sector indeed removes the additional constant shift such that the connected bosonic correlator is close to zero for $t/L \sim 1/2$. It is also worth discussing the rather oddly shaped fermionic correlation function. The figure reveals that there are contributions of four dominant exponentials instead of only one as in the unbroken case. For $t/L \sim 0$ and for $t/L \sim 1$, there are two separate exponentials with large slopes, one in forward direction and one in backward direction. We can interpret these parts as coming from the second mass gap of the fermion yielding an exponential decrease for small t and of the antifermion yielding an exponential increase for large t . In addition, we have two rather flat exponential contributions around $t/L \sim 1/2$. These can be interpreted as the first mass gaps for the fermion and antifermion. As discussed before, for broken supersymmetry the fermionic vacuum has a lower energy than the bosonic one due to lattice artefacts, and therefore the lowest mass gap for the fermion is in fact *negative* and leads to the increase around $t/L \sim 1/2$. The effective masses which are extracted in this region are very small. In fact, these are the first indications for the mass of the Goldstino which appears in the spectrum for broken supersymmetry. We will elaborate further on this

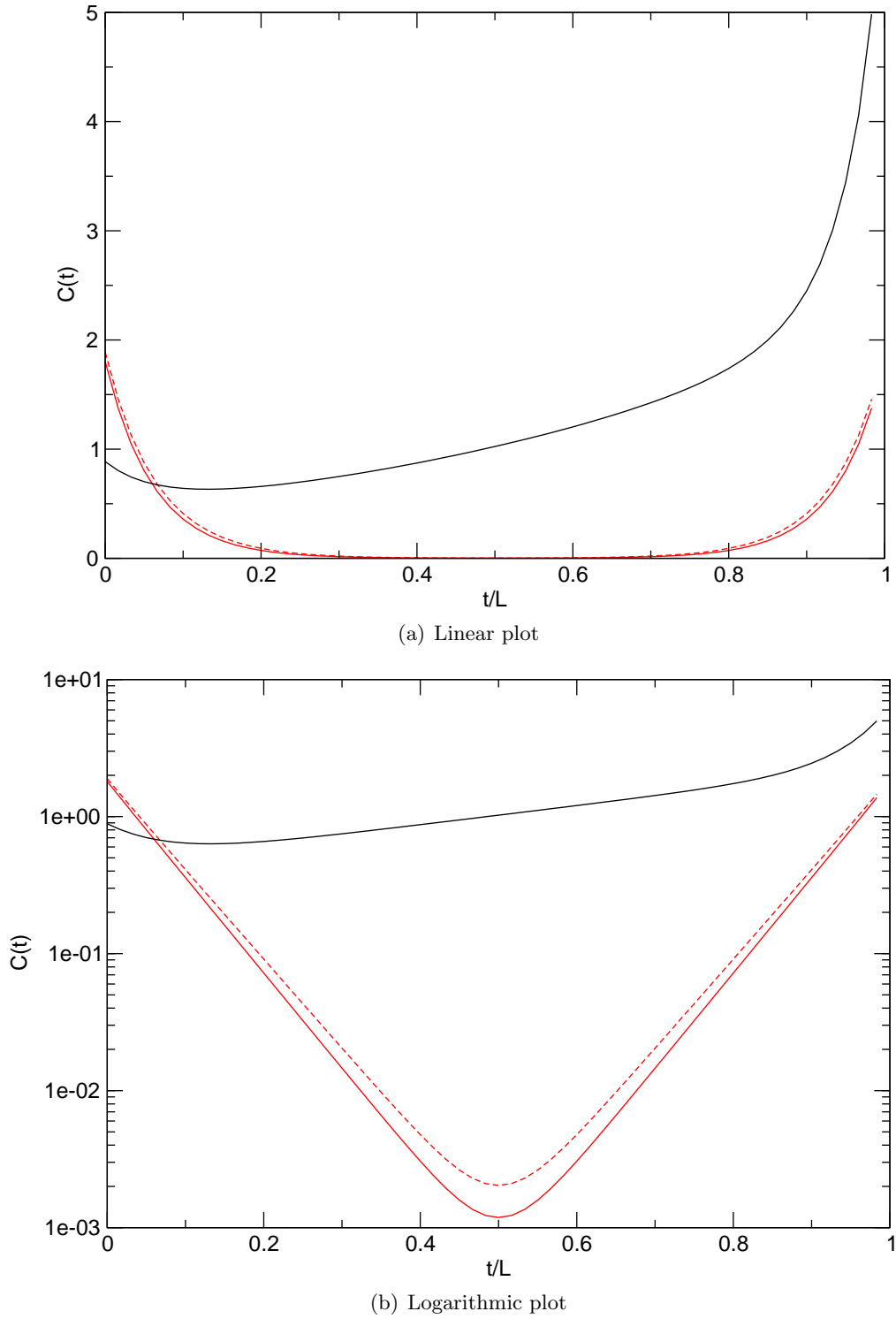


Figure 14: Broken supersymmetric quantum mechanics, standard discretisation. The bosonic (red) and fermionic (black) correlation functions in the sector Z_0 (solid line) and Z_1 (dashed line) at $\mu L = 10$ and $f_b = 1$.

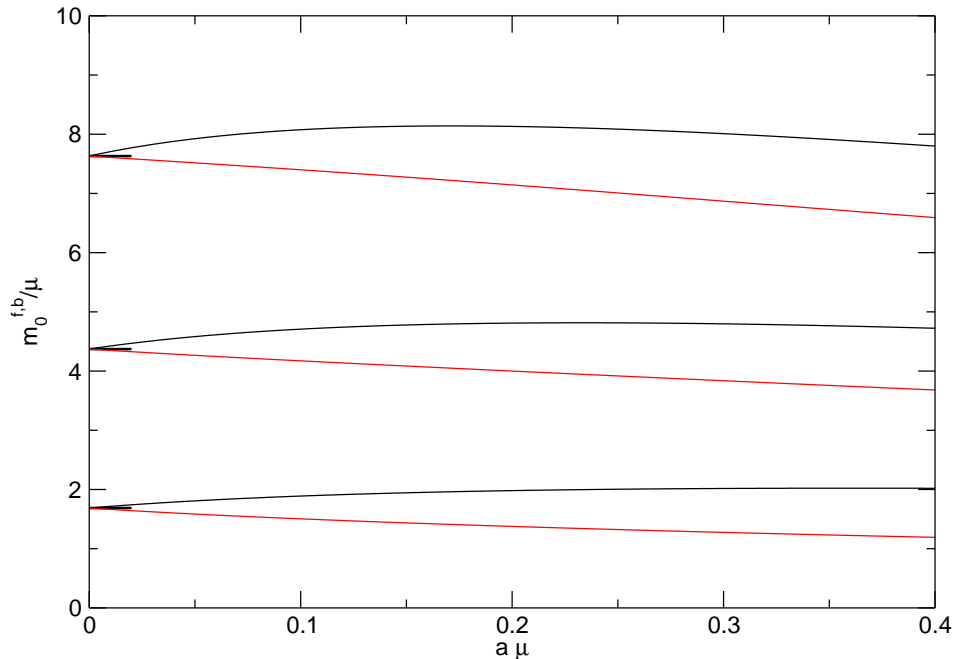


Figure 15: Unbroken supersymmetric quantum mechanics, standard discretisation. Continuum extrapolation of the bosonic (black) and fermionic (red) masses with respect to the bosonic vacuum at $f_u = 1$.

when we discuss the exact results for the mass gaps in the following section.

The correlation functions using the Q -exact discretisation do not reveal anything qualitatively different, hence we directly proceed to the discussion of the mass gaps where we can compare the lattice artefacts for the standard and Q -exact discretisation on a more quantitative level.

3.3 Mass gaps

The derivation of the mass gaps using the eigenvalues of the transfer matrices in Section 2.3 suggests to calculate the bosonic mass gaps in each sector separately. The fermionic mass gaps are measured via ratios of eigenvalues of T^1 and T^0 . This is a reflection of the fermionic correlation function being defined in the bosonic sector, but by reinterpreting the open fermion string in the bosonic sector as describing the antifermion string in the fermionic sector, one can also define the mass of an antifermion. In addition to our exact results at finite lattice spacing we also calculate the spectra directly in the continuum using Numerov's algorithm as a crosscheck and a benchmark for the lattice results. Since the spectrum is a property of the transfer matrix independent of the system size, the results do not depend on μL .

We start as usual with unbroken supersymmetry using the standard discretisation. In figure 15 we plot the bosonic and fermionic masses with respect to the bosonic vacuum at a coupling $f_u = 1$. First, we note that the mass gaps indeed extrapolate to the expected continuum values indicated by the horizontal lines at the left side of the plot. It turns out that the leading lattice artefacts are $\mathcal{O}(a)$ for both the fermion and boson masses but with opposite signs, and are reasonably small even at rather coarse lattice spacings. The mass

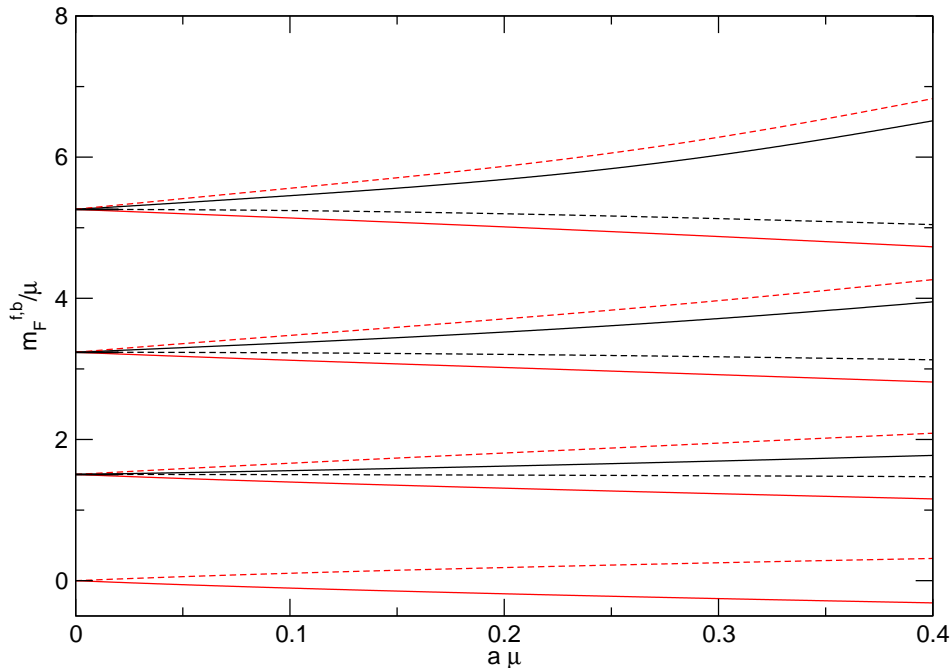


Figure 16: Broken supersymmetric quantum mechanics, standard discretisation. Continuum extrapolation of the bosonic (black) and fermionic (red) masses with respect to the bosonic (solid lines) and the fermionic (dashed lines) vacuum at $f_b = 1$.

gaps relative to the fermionic vacuum can of course also be calculated, but the information is redundant and we refer to [6] for the detailed results.

Next we discuss our exact results for broken supersymmetry using the standard discretisation. In figure 16, we display the results for the bosonic and the fermionic masses. While the fermionic vacuum is preferred over the bosonic one at finite lattice spacing, cf. figure 8, in the continuum they are on equal footing and contribute equally to the partition functions and observables. Hence in figure 16 we show the results for all the energy gaps, bosonic ones in black and fermionic ones in red, both with respect to the bosonic (solid lines) and fermionic vacuum (dashed lines), despite the fact that the results are partly redundant. In order to distinguish the lines we follow the notation in figure 5 where the energy levels for both sectors are depicted schematically for finite lattice spacing and in the continuum. It is important to note that the bosonic and the fermionic mass gaps extrapolate to the expected continuum values also for broken supersymmetry, and that the supersymmetry in the spectrum, i.e., the degeneracy between the bosonic and fermionic excitations, is restored in the continuum limit. This is in contrast to supersymmetric quantum field theories with spontaneously broken supersymmetry, where the spectrum becomes nondegenerate, see e.g. [7] for a nonperturbative demonstration in the two-dimensional $\mathcal{N} = 1$ Wess-Zumino model.

When supersymmetry is broken, one expects a fermionic zero-energy excitation, the Goldstino mode [8], which is responsible for the tunnelling between the bosonic and the fermionic vacuum and hence for the fact that $Z_p = 0$. From figure 16 it becomes clear how the lattice acts as a regulator for the Goldstino mode, namely by giving it a small mass of $\mathcal{O}(a)$, hence making it a would-be Goldstino. As a consequence, the Witten index W is regulated. This allows to give meaning to observables even in the system with broken supersymmetry and

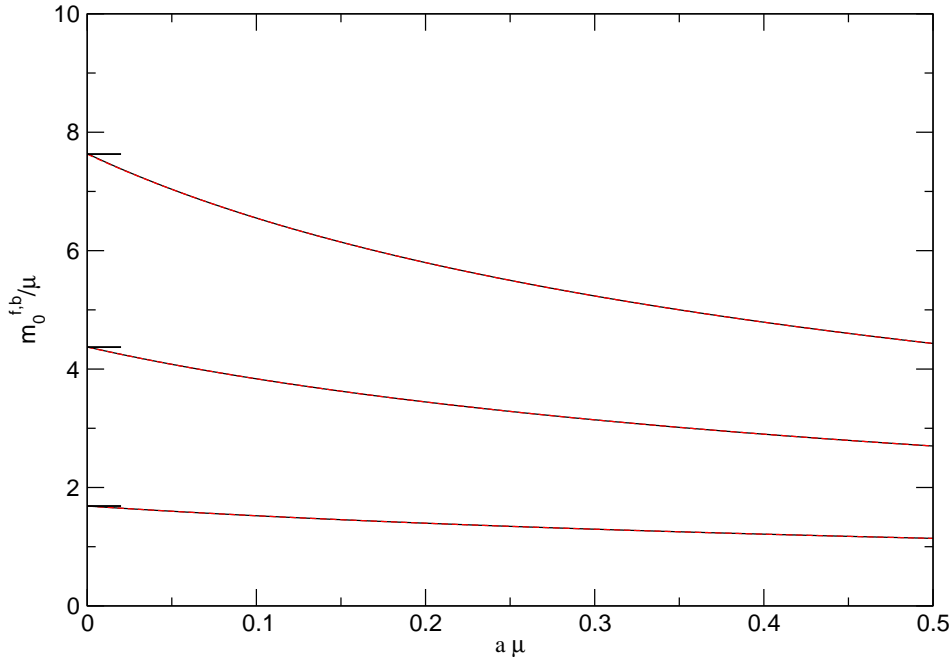


Figure 17: Unbroken supersymmetry, Q -exact discretisation. Continuum extrapolation of the bosonic masses measured with respect to the bosonic (black solid) and the fermionic (black dashed) vacuum and the fermionic masses measured with respect to the bosonic (red dashed) and the fermionic (red dotted) vacuum at $f_u = 1$.

periodic boundary conditions by defining them at finite lattice spacing, where Z_p is nonzero, and then taking the continuum limit. If the observable couples to the would-be Goldstino mode in the same way as Z_p does, both vanish in the continuum but their ratio is well defined. Note that since the fermionic vacuum has a lower energy than the bosonic one, the would-be Goldstino with positive mass is actually the antifermionic excitation $m_1^{\bar{f}}$ in the fermion sector, while the fermionic excitation m_0^f in the bosonic sector has a negative energy. A posteriori, this explains the rather odd shape of the fermionic correlation function in the bosonic sector displayed in figure 14 where the slope of the slowly increasing correlator corresponds to the small negative mass of the Goldstino fermion.

Finally, we make the observation that the leading lattice artefacts of the spectral mass gaps are all $\mathcal{O}(a)$. This is expected since we use a discretisation of the derivative with $\mathcal{O}(a)$ discretisation errors, both for the bosonic and fermionic degrees of freedom. However, it is intriguing that the linear artefacts of the higher lying bosonic mass gaps $m_{i,1}^b$ in the $F = 1$ sector become very small, and the corrections are eventually dominated by artefacts of $\mathcal{O}(a^2)$, i.e., some interesting conspiracy of lattice artefacts appears to cancel the $\mathcal{O}(a)$ artefacts.

Next we consider the spectrum using the Q -exact discretisation. In figure 17 we plot the fermionic (red) and bosonic mass gaps (black) with respect to the bosonic (full lines) and the fermionic vacuum (dashed lines) for unbroken supersymmetry with coupling $f_u = 1$. The characterisation of the lines is as in the previous figures for the mass gaps. From the figure it is clear that the degeneracy between the bosonic and fermionic excitations is maintained for any finite value of the lattice spacing. Apparently, keeping only half of the original symmetries in eq.(2), as realised by the Q -exact discretisation, is sufficient to guarantee the complete degeneracy. However, the lattice artefacts are rather different from the ones observed in the

spectrum of the standard discretisation. While the lattice artefacts in the lowest excitation are quantitatively comparable to the ones in the lowest fermionic excitation in the standard scheme, cf. figure 15, they turn out to be much larger for the higher excited states. As an example we find lattice corrections of up to 45% at a lattice spacing of $a\mu = 0.5$ for the third excited state. A possible explanation is that in order to maintain the exact degeneracy between the bosonic and fermionic energies, essentially aligning the lattice artefacts of the bosonic and fermionic states, the eigenvalues have to rearrange in a particular way and push the artefacts into the higher states. So while the Q -exact discretisation is an extremely useful scheme due to its improved symmetry properties, one has to be aware that the lattice artefacts may be dramatically enhanced for certain observables.

The spectrum of the Q -exact action for broken supersymmetry turns out to be very difficult to handle. On the one hand, using the superpotential P_b the transfer matrices T^0 and T^1 come out to be exactly similar when using a reasonably large cutoff for the bosonic occupation numbers and, hence, the energy levels are exactly degenerate for any lattice spacing. The similarity transformation relating the two transfer matrices can be understood as the supersymmetry transformation relating the bosonic and the fermionic sector and is exactly maintained at finite lattice spacing. As a consequence of the exact similarity we have an exactly massless Goldstino mode and hence also $Z_p/Z_a = 0$, independently of both the reasonably large occupation number cutoff and the lattice spacing a . On the other hand, however, results do not become independent of the cutoff even for reasonably large bosonic occupation numbers. Even on very small lattices and for coarse lattice spacings the occupation numbers necessary to produce stable transfer matrix eigenvalues appear to be extremely large. Hence, despite the fact that the properties of the transfer matrices qualitatively yield the correct physics in terms of the spectrum and the Witten index, we are not able to further investigate the system with broken supersymmetry using the Q -exact action.

3.4 Ward identities

In this section we present our exact results for the Ward identities which we introduced in Section 2.4. We discuss the identities W_0 , $W_1(t)$ and $W_2(t)$ in turn.

As usual we start with the discussion of the system with unbroken supersymmetry using the standard discretisation. In that case, the Ward identity W_0 in eq.(36) is supposed to vanish in the continuum limit. However, it turns out that the expectation value is trivially zero at any value of the lattice spacing, simply because in the bond formulation the \mathbb{Z}_2 -symmetry $\phi \rightarrow -\phi$ is exactly maintained for each bond configuration. This can most easily be seen from the fact that the site weights for this action are zero for an odd site occupation number, $Q_0(2n+1) = Q_1(2n+1) = 0$, $n \in \mathbb{N}_0$, and hence the expectation value of an odd power of ϕ trivially vanishes.

For broken supersymmetry, we need to check whether or not the Ward identity in eq.(39) vanishes. In figure 18, we plot the continuum extrapolation of $\langle P'_b \rangle$ for different values of μL at fixed coupling $f_b = 1$. For antiperiodic b.c., the Ward identity extrapolates to the value $\langle P' \rangle / \sqrt{\mu} = 0.3725 \dots$ independently of the chosen μL . This value is in agreement with a continuum calculation in the operator formalism [9] denoted by the horizontal dotted line at the left side of the plot. The continuum limit for periodic b.c., however, depends on the chosen μL and approaches the continuum value for antiperiodic b.c. only at large μL where the effects from the boundary become smaller and smaller. Note that the continuum limit for

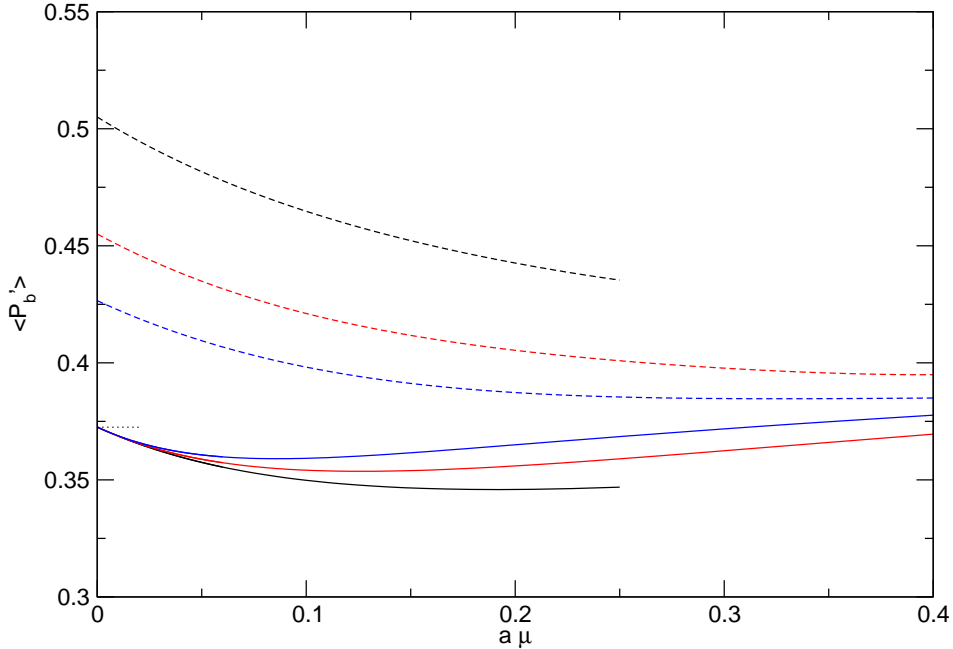


Figure 18: Broken supersymmetric quantum mechanics, standard discretisation. Continuum extrapolation of $\langle P'_b \rangle / \sqrt{\mu}$ for $\mu L = 5$ (black), $\mu L = 8$ (red), and $\mu L = 12$ (blue) using periodic (dashed lines) and antiperiodic b.c. (solid lines) at $f_b = 1$.

this quantity is well defined despite the fact that $Z_p = 0$ in that limit. In figure 19 we show the continuum values of W_0 for periodic b.c. as a function of $(\mu L)^{-1}$, i.e., the temperature in units of μ . The figure reveals that for large μL , the values for periodic b.c. indeed approach the ones for antiperiodic b.c. denoted by the dotted line. Eventually, the values agree in the zero temperature limit, or rather in the limit of infinite extent of the system. Interestingly, the finite temperature corrections seem to be described by the form $1/\mu L$ up to rather large values of μL . A corresponding fit is shown in figure 19 as the solid line. In conclusion, the Ward identity W_0 serves us indeed to verify that supersymmetry is broken in the continuum for the superpotential P_b .

The results for the Q -exact action do not provide any new interesting insights, because for unbroken supersymmetry W_0 vanishes trivially as for the standard discretisation. For broken supersymmetry we are not able to achieve stable results using the Q -exact action, as already discussed at the end of Section 3.3.

We now turn to the Ward identity W_1 to verify supersymmetry restoration and breaking for the corresponding superpotentials. We start again with the discussion of the results using the standard discretisation in the system with unbroken supersymmetry. In figure 20, we show the Ward identity $W_1(t)$ for $\mu L = 4$ and $\mu L = 10$ for a range of lattice spacings a/L at fixed coupling $f_u = 1$ for both periodic and antiperiodic boundary conditions. The figure illustrates how the Ward identity $W_1(t)$ is violated for finite lattice spacing. It can be seen that the violation for periodic b.c. becomes less severe as $a \rightarrow 0$, whereas for antiperiodic b.c. it does not. In figure 21, we plot the continuum extrapolation of $W_1(t/L = 1/2)$ at the coupling $f_b = 1$ for different values of μL . We find that $W_1(t/L = 1/2)$ extrapolates to zero for periodic b.c., independent of the value of μL . Supersymmetry is therefore restored in the continuum for periodic b.c., even at a finite extent of the quantum mechanical system. For

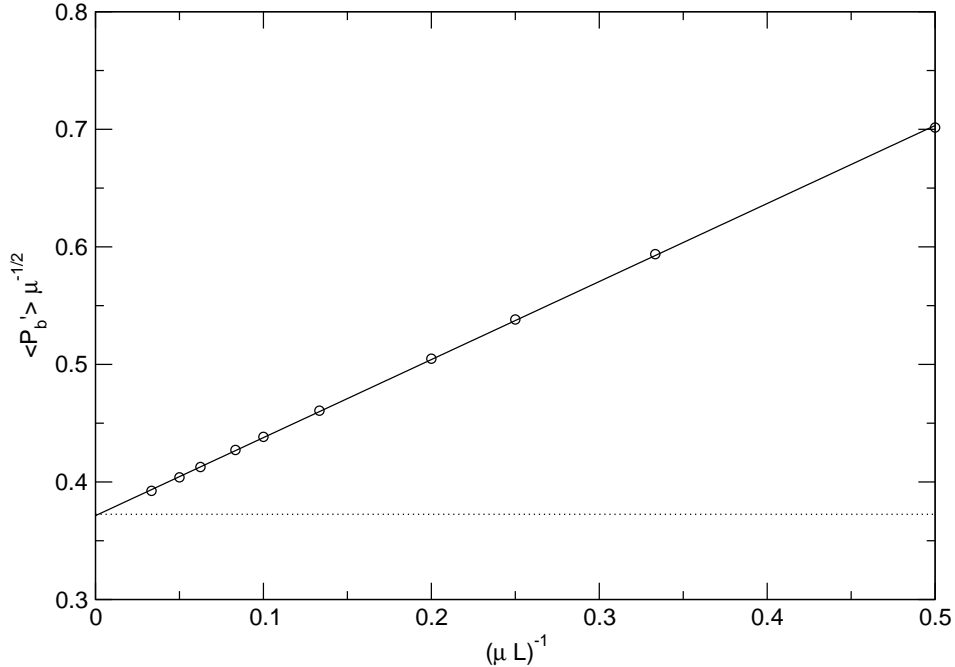


Figure 19: Broken supersymmetric quantum mechanics. The continuum values for $\langle P'_b \rangle / \sqrt{\mu}$ as a function of $1/\mu L$ for periodic b.c. at $f_b = 1$. The continuum value for antiperiodic b.c. is indicated with the black dotted line. The solid black line is a fit linear in $1/\mu L$.

antiperiodic b.c. on the other hand, $W_1(t/L = 1/2)$ does not extrapolate to zero for small μL , i.e., high temperature. However, as the temperature decreases, the violation weakens and for $\mu L \rightarrow \infty$ $W_1(t/L = 1/2)$ extrapolates to zero, implying that supersymmetry is restored in the zero temperature limit. On the level of the Ward identities W_1 in the continuum, our results hence confirm all expected features of unbroken supersymmetry at finite as well as at zero temperature. Moreover, our results tell us how the system behaves at finite lattice spacing. First we note that at any fixed lattice spacing, W_1 extrapolates to zero in the limit $\mu L \rightarrow \infty$ independently of the boundary conditions. This is a reflection of the fact that the violation of the supersymmetry in the action from using the standard discretisation is just a surface term which obviously becomes irrelevant in the limit $\mu L \rightarrow \infty$. On the other hand, we note that the decoupling of this artefact seems to happen faster in a system with antiperiodic boundary conditions. In other words, the convergence to $W_1 = 0$ is slower for periodic b.c. as can be seen by comparing the limit $\mu L \rightarrow \infty$ for example at fixed $a\mu = 0.15$.

Next, we consider the Ward identity W_1 for broken supersymmetry using the standard discretisation. In figure 22, we show W_1 for $\mu L = 5$ and $\mu L = 10$ for a range of lattice spacings a/L at fixed coupling $f_b = 1$ both for periodic and antiperiodic boundary conditions. This figure illustrates how the Ward identity W_1 is violated for broken supersymmetry at finite lattice spacing. However, unlike in the previous case of unbroken supersymmetry, the violation of the Ward identity W_1 remains finite even when the lattice spacing or the temperature goes to zero. To illustrate this further, we trace the Ward identity $W_1(t/L = 3/4)$ into the continuum for different μL in figure 23. Clearly, the violation persists in the continuum, independently of the boundary conditions and the size or temperature of the system. In this case too, all features of broken supersymmetry are numerically confirmed on the level of the

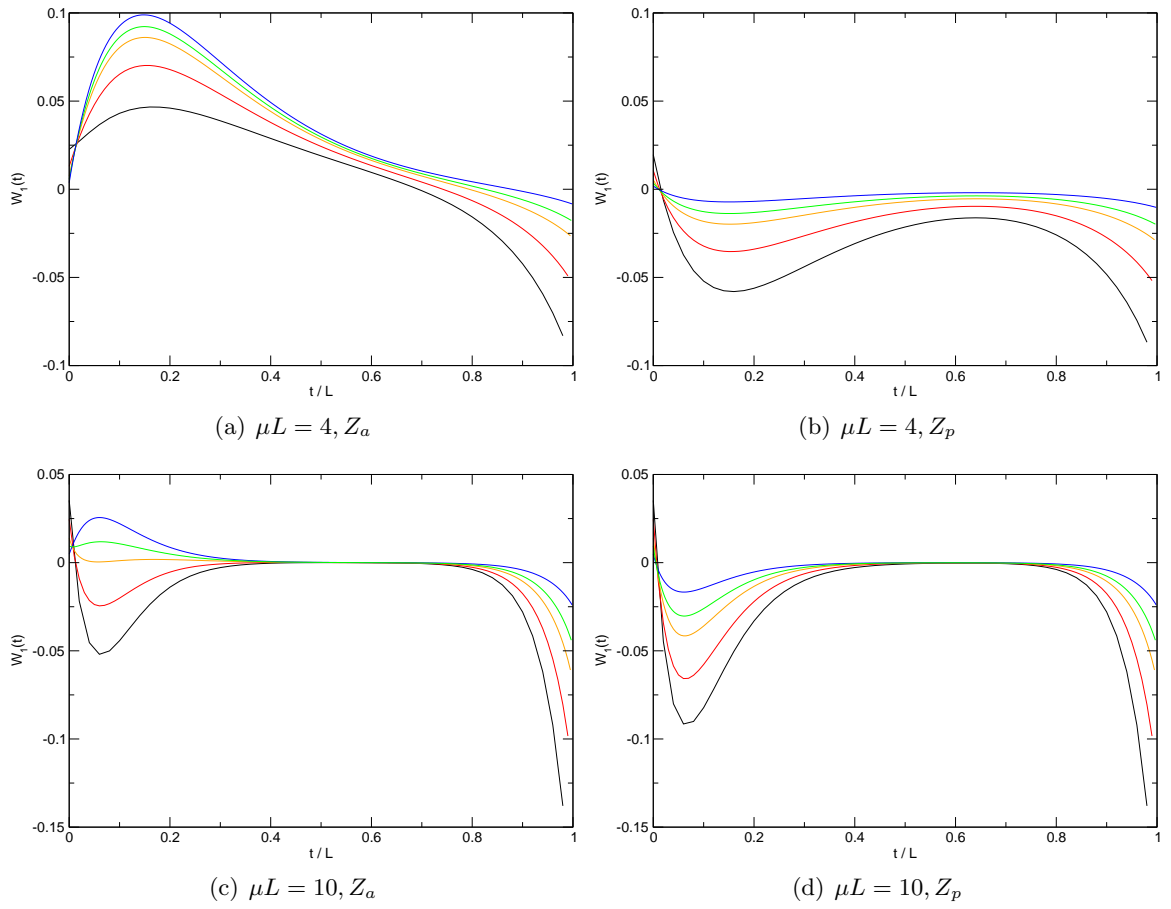


Figure 20: Unbroken supersymmetric quantum mechanics, standard discretisation. The Ward identity W_1 for $L/a = 50$ (black), $L/a = 100$ (red), $L/a = 200$ (orange), $L/a = 300$ (green) and $L/a = 600$ (blue) for $\mu L = 4$ and $\mu L = 10$ at fixed coupling $f_u = 1$.

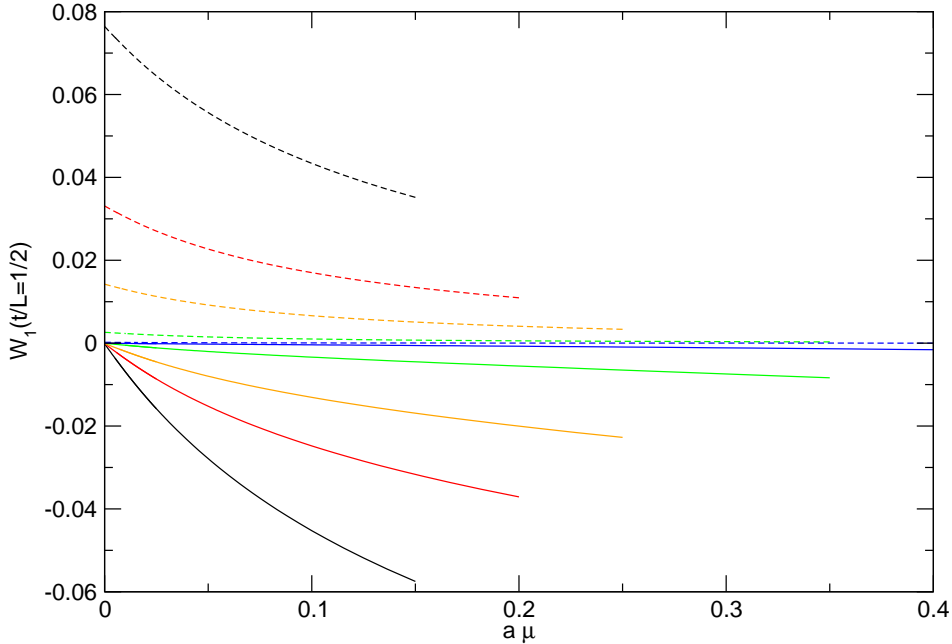


Figure 21: Unbroken supersymmetric quantum mechanics, standard discretisation. Continuum extrapolation of $W_1(t/L = 1/2)$ for $\mu L = 3$ (black), $\mu L = 4$ (red), $\mu L = 5$ (orange), $\mu L = 7$ (green) and $\mu L = 10$ (blue) for periodic (solid lines) and antiperiodic b.c. (dashed lines) at fixed coupling $f_b = 1$.

Ward identity W_1 .

Next we consider the Ward identity W_1 for unbroken supersymmetry using the Q -exact discretisation. In this case W_1 is of special interest since for this action $\delta_1 S_L^Q = 0$ at finite lattice spacing, and we should hence be able to confirm that $W_1(t) = 0 \forall t$ at finite lattice spacing for unbroken supersymmetry and periodic boundary conditions. In figure 24 we show the Ward identity W_1 at different values of the lattice spacing a/L at fixed coupling $f_u = 1$ and fixed extent $\mu L = 10$ for both periodic and antiperiodic boundary conditions. The plot shows that the Ward identity W_1 represented by the dashed line is indeed zero $\forall t$ using periodic boundary conditions at any finite lattice spacing. Note, that $W_1(t)$ is composed of the bosonic and fermionic correlators as given in eq.(36) and is in fact nontrivially zero. For antiperiodic b.c. on the other hand, the violation of the Ward identity at finite temperature is evident. To observe the behaviour of the Ward identity W_1 in the zero temperature limit, in Fig. 25 we again trace $W_1(t/L = 1/2)$ into the continuum for different μL . Of course, for periodic b.c. $W_1(t/L = 1/2)$ is zero for any finite $a\mu$ and any value of μL (dashed lines). However, for antiperiodic b.c., the extrapolation of $W_1(t/L = 1/2)$ shows a dependence on μL , but in the limit $\mu L \rightarrow \infty$ this violation also vanishes, as expected.

We now perform the same analysis for the Ward identity W_2 given in eq.(35). This Ward identity is not expected to vanish for finite lattice spacing, since the action S_L^Q is not invariant under the supersymmetry transformation δ_2 . In figure 26 we show $W_2(t)$ for different lattice spacings a/L for $\mu L = 10$ at fixed coupling $f_u = 1$. As expected, this Ward identity is violated for both periodic and antiperiodic b.c. at finite lattice spacing and for finite temperature. To observe the continuum behaviour, we trace $W_2(t/L = 1/2)$ in this case, too. The continuum extrapolation for different μL is shown in figure 27. For periodic b.c., the violation of the Ward identity $W_2(t/L = 1/2)$ vanishes in the continuum independently of the chosen μL .

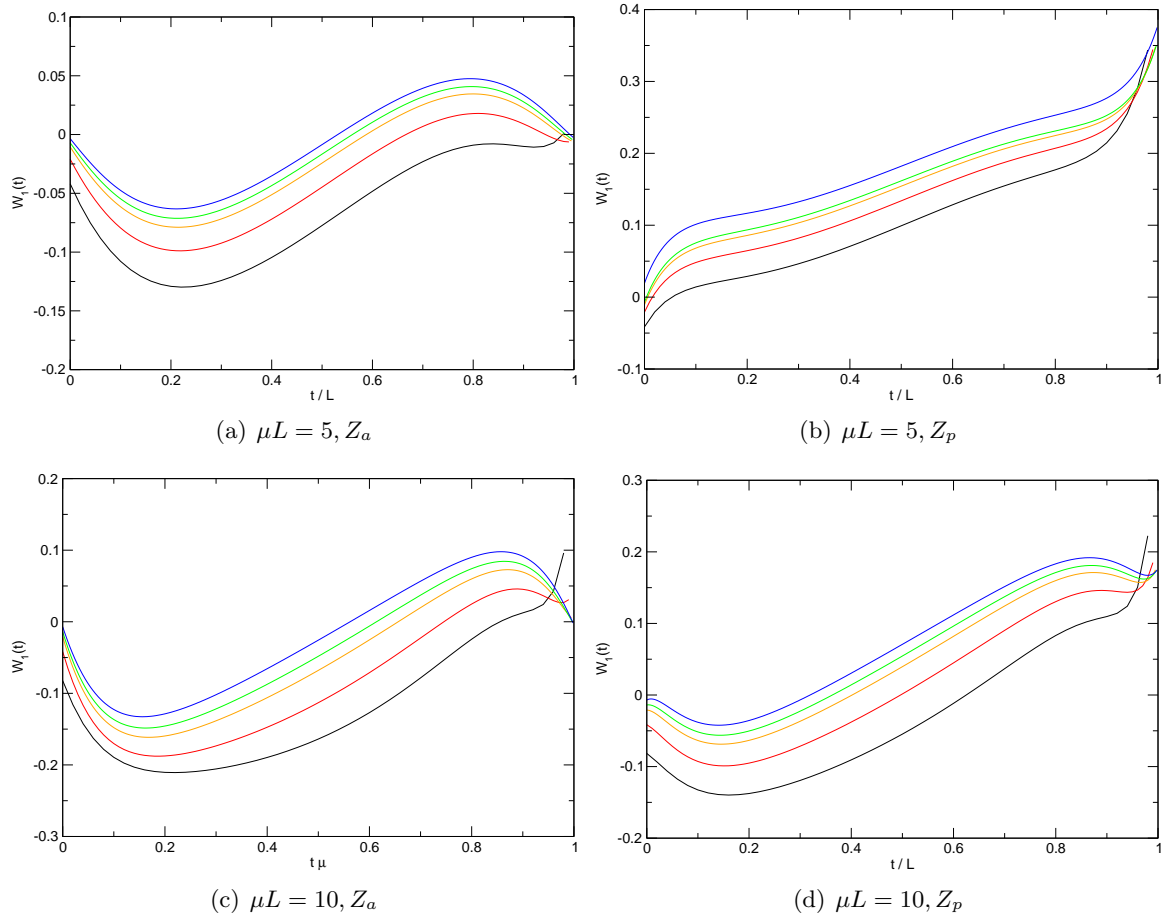


Figure 22: Broken supersymmetric quantum mechanics, standard discretisation. The Ward identity W_1 for $L/a = 50$ (black), $L/a = 100$ (red), $L/a = 200$ (orange), $L/a = 300$ (green) and $L/a = 600$ (blue) for $\mu L = 5$ and $\mu L = 10$ at fixed $f_b = 1$.

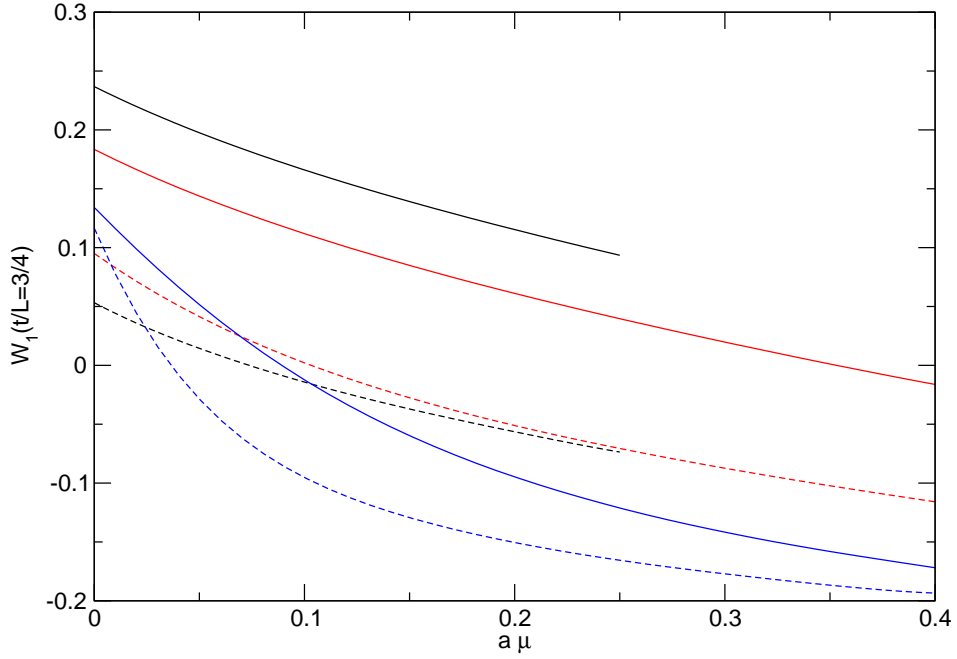


Figure 23: Broken supersymmetric quantum mechanics, standard discretisation. Continuum extrapolation of $W_1(t/L = 3/4)$ for $\mu L = 5$ (black), $\mu L = 10$ (red) and $\mu L = 20$ (blue) for periodic (solid lines) and antiperiodic b.c. (dashed lines) at fixed coupling $f_b = 1$.

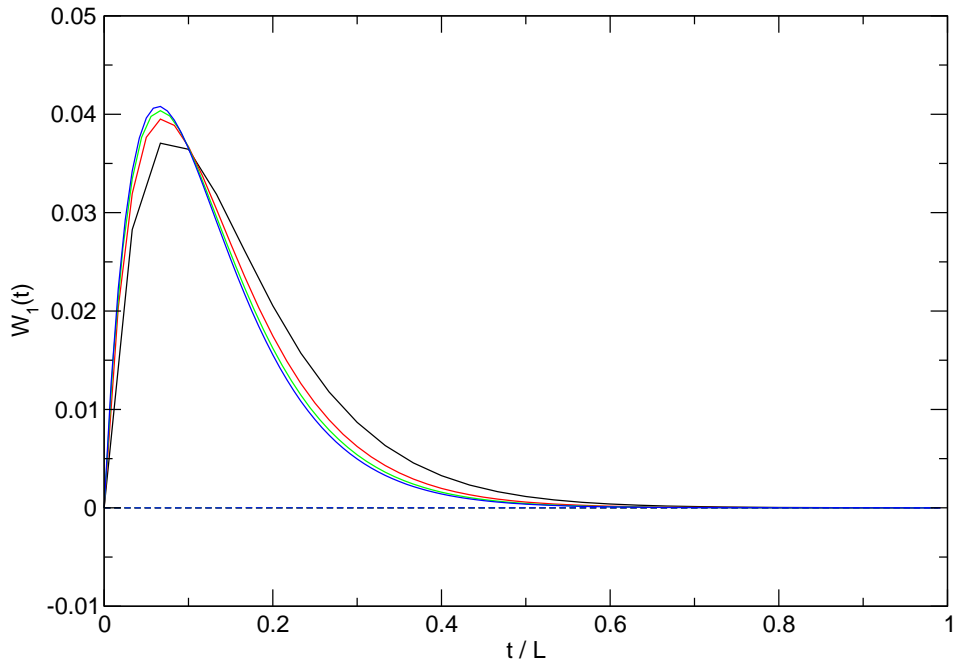


Figure 24: Unbroken supersymmetric quantum mechanics, Q -exact discretisation. The Ward identity $W_1(t)$ for $L/a = 30$ (black), $L/a = 60$ (red), $L/a = 90$ (green) and $L/a = 120$ (blue) for antiperiodic (solid lines) and periodic b.c. (dashed lines) for $\mu L = 10$ at fixed coupling $f_u = 1$.

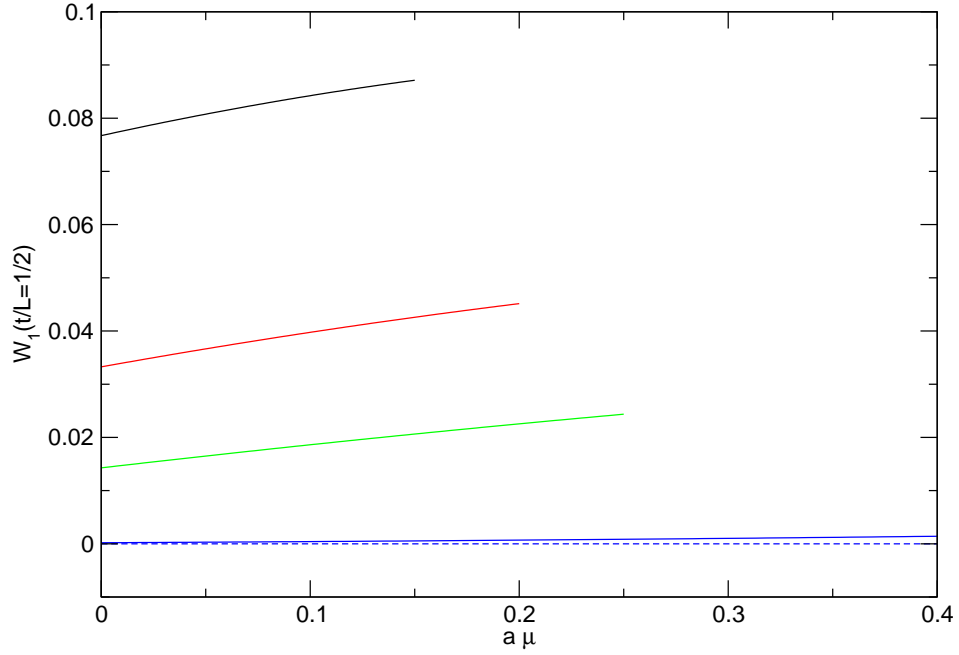


Figure 25: Unbroken supersymmetric quantum mechanics, Q -exact discretisation. Continuum extrapolation of $W_1(t/L = 1/2)$ for $\mu L = 3$ (black), $\mu L = 4$ (red), $\mu L = 5$ (green) and $\mu L = 10$ (blue) for antiperiodic (solid lines) and periodic b.c. (dashed lines) at fixed coupling $f_b = 1$.

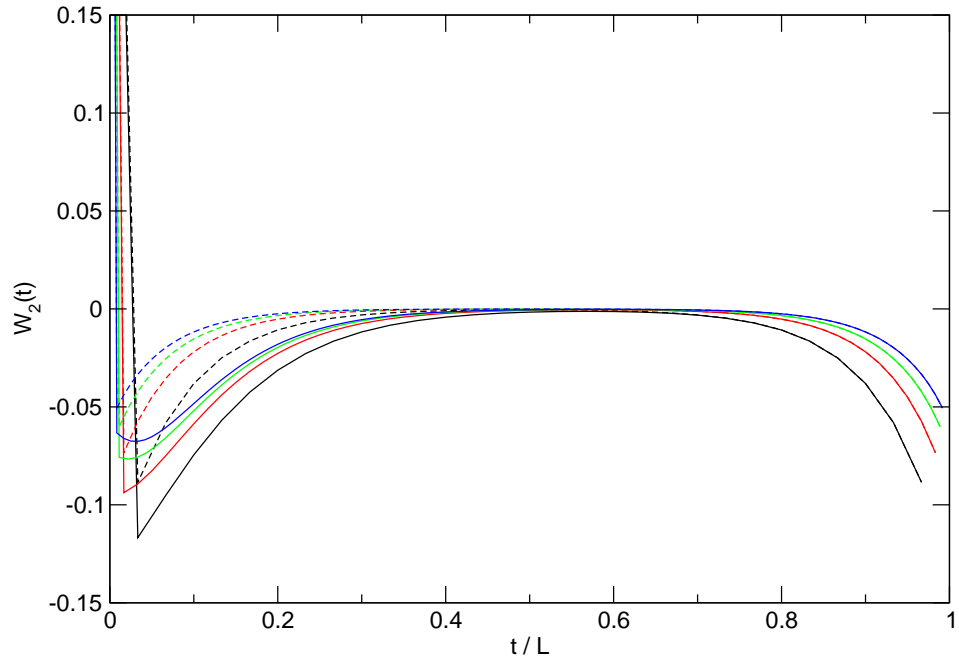


Figure 26: Unbroken supersymmetric quantum mechanics, Q -exact discretisation. The Ward identity W_2 for $L/a = 30$ (black), $L/a = 60$ (red), $L/a = 90$ (green) and $L/a = 120$ (blue) for antiperiodic (solid lines) and periodic b.c. (dashed lines) for $\mu L = 10$ at fixed coupling $f_u = 1$.

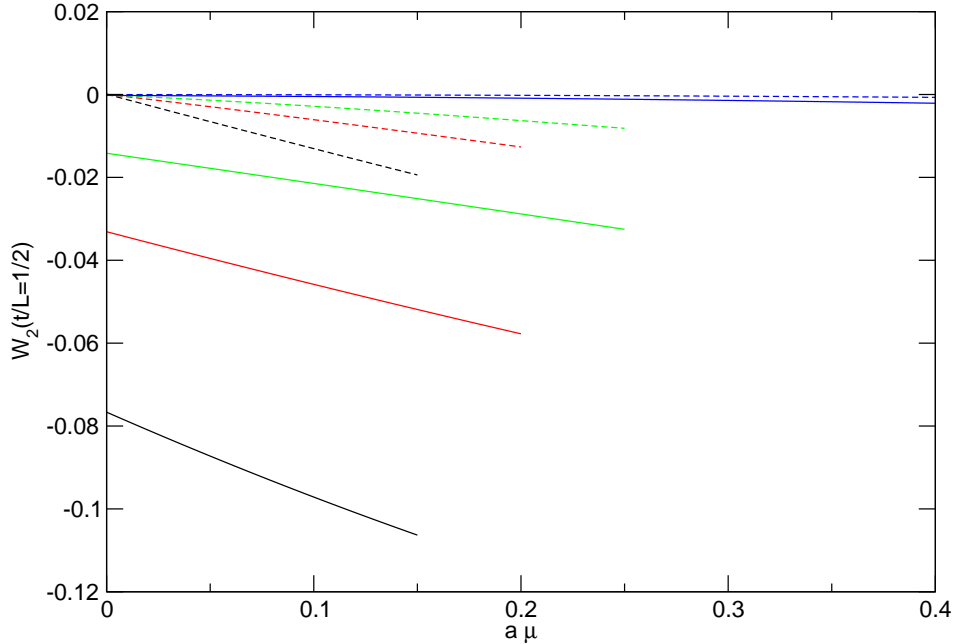


Figure 27: Unbroken supersymmetric quantum mechanics, Q -exact discretisation. Continuum extrapolation of $W_2(t/L = 1/2)$ for $\mu L = 3$ (black), $\mu L = 4$ (red), $\mu L = 5$ (green) and $\mu L = 10$ (blue) for antiperiodic (solid lines) and periodic b.c. (dashed lines) at fixed coupling $f_u = 1$.

The restoration of supersymmetry in the continuum is thus also confirmed via the Ward identity $W_2(t/L = 1/2)$. For antiperiodic b.c. however, the violation does not vanish for small μL . Again, this is just a reflection of the fact that the finite temperature breaks the supersymmetry, and it is only restored in the zero temperature limit. Hence, on the level of the Ward identities W_1 and W_2 , all the features of unbroken supersymmetry formulated with the Q -exact action are numerically confirmed. Analogously to the standard discretisation $W_2(t/L = 1/2)$ extrapolates to zero at any value of the lattice spacing, independent of the employed boundary conditions. This confirms that the violation of the supersymmetry δ_2 in the Q -exact formulation is just a boundary term which decouples from the system in the limit $\mu L \rightarrow \infty$.

3.5 The ground state energy E_0

In this section we follow [10] and measure the ground state energy E_0 for the Q -exact action via the expectation value of an appropriate Hamilton operator H . In a field theory it is a priori not clear how to measure an absolute energy and there are in fact several possible candidate Hamilton operators which differ from each other by constant shifts. However, the authors of [10] argue via the off-shell formulation of the theory, that constructing the Hamilton operator from the Q -exact action leads to the correct measurement of the ground state energy. In the lattice formulation, it reads

$$H = -\frac{1}{2}(\Delta^- \phi)^2 + \frac{1}{2}(P')^2 - \frac{1}{2}\bar{\psi}(\Delta^- - P'')\psi. \quad (45)$$

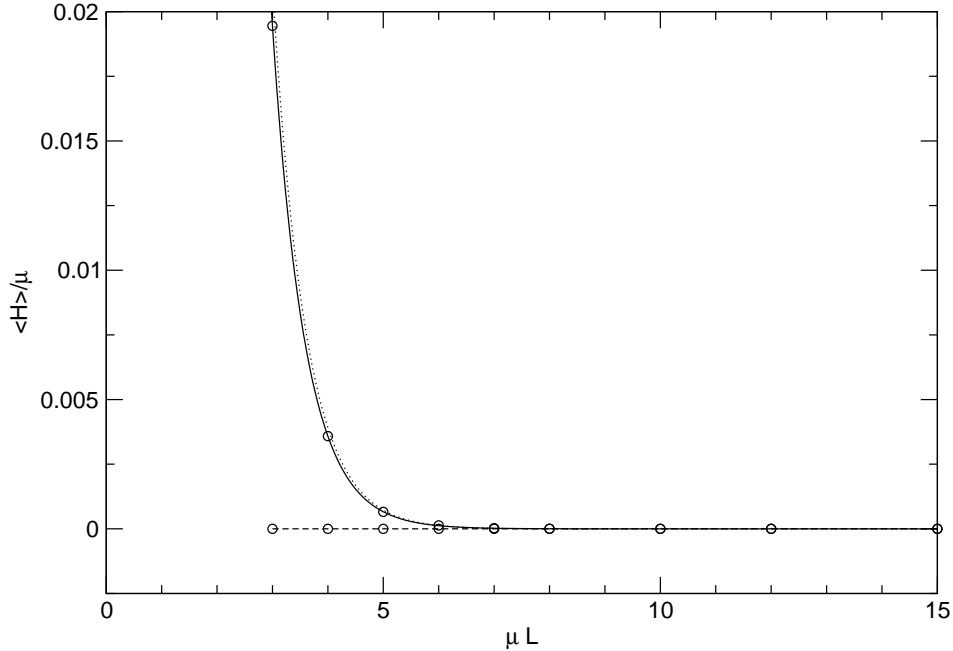


Figure 28: Unbroken supersymmetric quantum mechanics, Q -exact action. Continuum values of $\langle H \rangle / \mu = E_0 / \mu$ for periodic (dashed line) and antiperiodic b.c. (solid line) for a range of system sizes μL at fixed coupling $f_u = 1$. The dotted line describes the leading asymptotic behaviour for large μL while the full line is a phenomenological fit.

Using the superpotential P_u in eq.(3), the expectation value of this Hamilton operator is explicitly given by

$$\begin{aligned} \langle H \rangle &= \frac{1}{2}(\mu^2 - 2)\langle \phi^2 \rangle + \mu g \langle \phi^4 \rangle + \frac{1}{2}g^2 \langle \phi^6 \rangle + \langle \phi_1 \phi_0 \rangle \\ &+ \frac{1}{2}(\mu - 1)\langle \bar{\psi} \psi \rangle + \frac{1}{2}\langle \bar{\psi}_1 \psi_0 \rangle + \frac{3}{2}g^2 \langle \bar{\psi} \psi \phi^2 \rangle. \end{aligned} \quad (46)$$

In figure 28 we show the continuum values for $\langle H \rangle / \mu$ for different μL for both periodic and antiperiodic b.c. at a coupling $f_u = 1$. For periodic b.c. the operator H yields zero independently of the lattice spacing a/L and μL . Here, too, this zero is nontrivial, since it emerges from an exact cancellation of the various expectation values in eq.(46). For antiperiodic b.c. the continuum values show an exponentially decreasing behaviour with μL and the expectation value $\langle H \rangle / \mu$ goes to zero only in the limit $\mu L \rightarrow \infty$. The exponential behaviour can easily be inferred from expanding the expectation value in terms of the energy states. Taking only the lowest mass gap into account one obtains

$$\langle H \rangle = \frac{2 m_1^b e^{-m_1^b L}}{1 + 2 e^{-m_1^b L}}. \quad (47)$$

The dotted line in figure 28 corresponds to this expression with $m_1^b / \mu = 1.6865$, in agreement with our results in section 3.3. The full line is a phenomenological fit using m_1^b in eq.(47) as an effective fit parameter which also takes into account additional contributions from higher excitations. In conclusion, our exact results confirm the arguments presented in [10].

4 Conclusions and outlook

In this paper we have presented exact results for $\mathcal{N} = 2$ supersymmetric quantum mechanics discretised on the lattice. Expressing the bosonic and fermionic degrees of freedom in terms of bosonic and fermionic bonds, respectively, allows to completely characterise the system by means of transfer matrices defined separately in the bosonic and fermionic sector. From the properties of the transfer matrices one can derive exact results for all observables at finite lattice spacing and we present such results for a variety of interesting observables using two different discretisation schemes. The first is the standard discretisation which involves a Wilson term for the fermions and a counterterm which guarantees the restoration of supersymmetry in the continuum. The second discretisation is a Q -exact one which maintains one of the two supersymmetries exactly at finite lattice spacing [4]. The exact calculations allow to study in detail how the continuum limit $a\mu \rightarrow 0$ as well as the thermodynamic limit $\mu L \rightarrow \infty$ are approached and how the two limits interfere with each other. The latter of the two limits can be interpreted as the zero temperature limit in a system with antiperiodic b.c. for the fermion. Since the supersymmetry of the system can be broken both by the finite lattice spacing and the finite temperature the interplay of the two limits is of particular interest in order to gain a complete understanding of the various lattice discretisation schemes.

For the ratio of partition functions Z_p/Z_a , which is proportional to the Witten index, we find for example the interesting result that in a system with broken supersymmetry, where the Witten index is supposed to vanish, it extrapolates to -1 in the zero temperature limit at any finite lattice spacing. On the other hand, it extrapolates to 0 in the continuum limit for any finite temperature or extent of the system. In fact it turns out that the lattice spacing corrections are exponentially enhanced towards the low temperature limit, so in this case the order of the limits is crucial to describe the correct physics in the continuum. It is also interesting to study the influence of the finite lattice spacing on the fermionic and bosonic two-point correlation functions. In particular, for broken supersymmetry one expects the emergence of a massless Goldstino mode and within our approach we can study in detail how the mode expresses itself in the fermionic correlation function. Moreover, we study the bosonic and fermionic spectrum of the theory which allows to better quantify the lattice corrections. We demonstrate how the degeneracy between the bosonic and fermionic excitations is restored in the continuum both for broken and unbroken supersymmetry when the standard discretisation scheme is used. For broken supersymmetry we see how the finite lattice spacing regulates the Goldstino mode and hence also the vanishing Witten index. Although the coupling strengths we study are well in the nonperturbative regime, the leading lattice corrections in the spectrum turn out to be reasonably small and follow the usual expectations of being $\mathcal{O}(a)$ to leading order. For the Q -exact discretisation scheme we find exact degeneracy between the fermionic and bosonic excitations at any finite lattice spacing. It seems that maintaining only one of the supersymmetries on the lattice is sufficient to guarantee the exact degeneracy. In this case, too, the lattice artefacts are $\mathcal{O}(a)$ to leading order, but appear to be enhanced with respect to the standard discretisation, in particular for the higher lying excitations.

We are also able to study in detail the behaviour of various Ward identities towards the continuum and thermodynamic limits for both discretisation schemes. Our exact results show that the finite lattice spacing and finite temperature effects can sometimes be rather large, but nevertheless both supersymmetries are completely restored in the appropriate limits without

any surprises. The Ward identities W_1 and W_2 play a particularly important role for the Q -exact discretisation. Since in that case half of the supersymmetries is exactly maintained, some of the Ward identities are expected to be fulfilled at finite lattice spacing for periodic boundary conditions. We prove numerically that this is indeed the case. Finally, for the Q -exact discretisation we also demonstrate the correctness of the conjecture in [10, 11] which provides a scheme to calculate the ground state energy.

In conclusion, we now have a rather complete qualitative and quantitative understanding of the interplay between infrared and ultraviolet effects in supersymmetric quantum mechanics regulated on a lattice of finite extent and finite lattice spacing. Moreover, our exact results provide a benchmark for any attempt to deal with supersymmetric field theories using a new discretisation scheme, or in fact even for any new regularisation scheme such as, e.g., the one described in [12]. In addition, new simulation algorithms specific to supersymmetric theories can be tested against our exact results. For example, there exist particular algorithms which are tailored to efficiently simulate bond occupation numbers, be they bosonic [13] or fermionic [14]. In fact, in the third paper of our series [5] we present the practical application of the so-called open fermion string algorithm to supersymmetric quantum mechanics in the bond formulation and prove its feasibility to deal numerically with the sign problem associated with broken supersymmetry. Our exact results here provide the necessary background to assess the validity and success of the numerical simulations using the fermion loop approach. Similarly, alternative approaches which attempt or claim to solve fermion sign problems, such as the ones in [15–17], can be tested in supersymmetric quantum mechanics and gauged against the exact results presented here.

An important question is of course whether the bond formulation and transfer matrix approach outlined here can be extended and applied to more complicated systems. This is indeed possible as we demonstrated in [18] where the fermion loop approach is applied to supersymmetric Yang-Mills quantum mechanics. In that system, transfer matrices describing the fermionic degrees of freedom can also be constructed explicitly in each sector with fixed fermion number and it is shown how they are related to the standard canonical approach. It is interesting to note that, despite the model involving a gauge degree of freedom, the transfer matrix approach can be extended to handle also this situation. Concerning the extension of the approach to higher dimensions the perspectives are not so bright. Up to a few exceptions, it is in general not possible or practical to construct transfer matrices for systems in higher dimensions. In contrast, the fermion loop formulation can be used on its own, e.g. [19, 20], and in some cases even provides the basis for the solution of the fermion sign problem such as in the $\mathcal{N} = 1$ Wess-Zumino model [7, 21].

A Technical aspects

A.1 Cutoff procedure for the bond occupation numbers

In this appendix we briefly describe and illustrate our procedure to choose an appropriate cutoff for the bond occupation numbers. The introduction of the cutoff is necessary in order to construct transfer matrices of finite size, such that they can be handled numerically. In the bond formulation the weights involving large bond occupation numbers are suppressed by factors of $1/n_i^{b_i!}$, so their contributions become irrelevant as the occupation numbers grow.

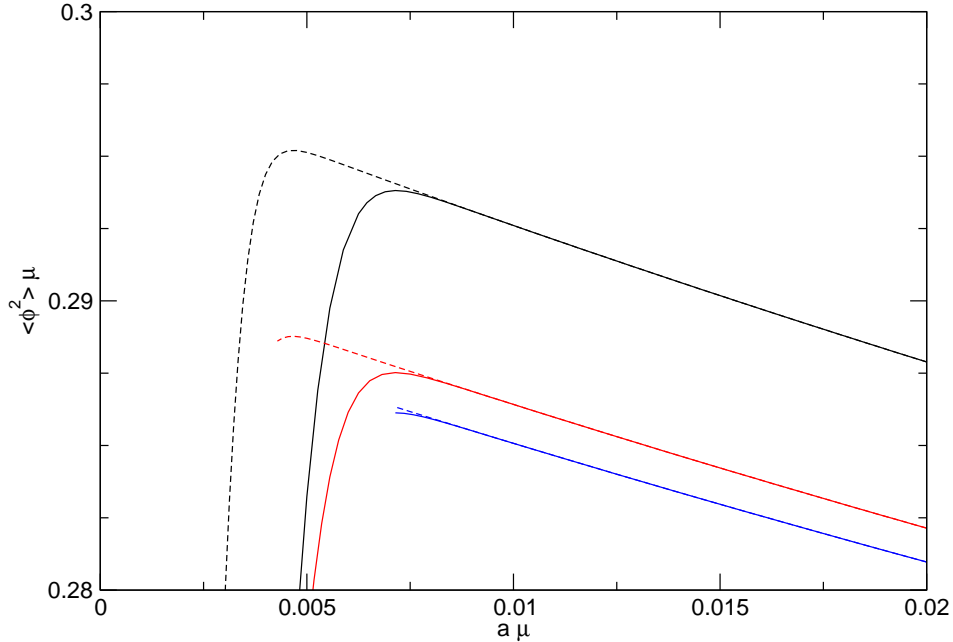


Figure 29: $\langle \phi^2 \rangle_a \cdot \mu$ as a function of $a\mu$ at fixed coupling $f_u = 1$ for different $\mu L = 2$ (black), $\mu L = 3$ (red), and $\mu L = 5$ (blue) and $N_{1 \rightarrow 1}^{cut} = 800$ (dashed line) and $N_{1 \rightarrow 1}^{cut} = 500$ (solid line). Effects from the finite cutoff on the bosonic bond occupation numbers near the continuum are clearly visible.

The truncation of the hopping expansion hence provides a natural and systematic scheme to limit the size of the transfer matrices.

For the standard discretisation we only have one type of bosonic bond $b_{1 \rightarrow 1}$ and hence the size of the transfer matrix grows linearly with the cutoff $N_{1 \rightarrow 1}^{cut}$ on the occupation number $n_{1 \rightarrow 1}^b$. Calculating an observable at different lattice spacings with varying cutoff $N_{1 \rightarrow 1}^{cut}$, effects from the finite bosonic cutoff manifest themselves as a sudden bend in an otherwise linear curve close to the continuum. In figure 29 we show an example of this effect by means of the expectation value $\langle \phi^2 \rangle_a \cdot \mu$ for antiperiodic b.c. and unbroken supersymmetry as a function of the lattice spacing $a\mu$ for different values of μL at fixed coupling $f_u = 1$. The effect of the finite cutoff for the bond occupation numbers is illustrated by comparing the observable for two different cutoffs, $N_{1 \rightarrow 1}^{cut} = 800$ and $N_{1 \rightarrow 1}^{cut} = 500$ close to the continuum. The curves for the expectation value are indistinguishable for $a\mu \gtrsim 0.075$, but closer to the continuum, the curve for the smaller cutoff suddenly diverges from the curve for the larger cutoff, and the values obtained using the lower cutoff are no longer reliable. For the larger cutoff a similar effect appears at a smaller lattice spacing, but is again clearly visible. So for any given cutoff, the results are reliable only down to a specific lattice spacing, which however is easy to determine since the cutoff effects are so dramatic. It turns out that for the observables considered in this paper, a cutoff $N_{1 \rightarrow 1}^{cut} = 800$ is sufficient to safely reach a lattice spacing $a\mu \sim 0.005$, well in the regime where the dominating lattice artefacts are of order $\mathcal{O}(a)$ and the corrections of $\mathcal{O}(a^2)$ are very small. It is then safe to extrapolate the data to the continuum by fitting a quadratic function

$$f(x) = c_0 + c_1 x + c_2 x^2 \quad (48)$$

to the data with $a\mu \gtrsim 0.005$ while making sure that the data is not affected by a change of the cutoff around $N_{1 \rightarrow 1}^{cut} = 800$. For almost all observables, these fits can be performed without

any difficulties. In cases where the lattice artefacts turn out to be particularly large, higher corrections can be taken into account without any problems and we indicate in the discussion when we do so.

For the Q -exact discretisation, we have two types of bosonic bonds $b_{1 \rightarrow 1}$ and $b_{1 \rightarrow \nu}$ and we need to introduce two cutoffs $N_{1 \rightarrow 1}^{cut}$ and $N_{1 \rightarrow \nu}^{cut}$ on the corresponding occupation numbers, hence the size of the transfer matrices grows quadratically in the cutoff, i.e., as $N_{1 \rightarrow 1}^{cut} \cdot N_{1 \rightarrow \nu}^{cut}$. Nevertheless, it turns out that also in this case the onset of cutoff effects in the observables is clearly indicated by a sudden bend away from the leading (linear) behaviour expected towards the continuum $a\mu \rightarrow 0$. Typically we choose the cutoffs $N_{1 \rightarrow 1}^{cut} = 64$ and $N_{1 \rightarrow \nu}^{cut} = 16$ for our calculations, yielding transfer matrices of size 1105×1105 . For the extrapolations, we proceed analogously to the case with the standard discretisation and we find that extrapolating the exact results with quadratic fits allows for reliable continuum results for the Q -exact discretisation, too.

A.2 Construction of the transfer matrix elements

In this appendix we briefly comment on the construction of the transfer matrices. As we emphasised at the end of Section 2.1, the evaluation of the site weights $Q_F(N)$ tends to be numerically unstable for large values of N . In the third paper of our series [5] we will discuss an algorithm which allows to reliably calculate the ratios

$$R'_F(N) \equiv \frac{Q_F(N+1)}{Q_F(N)}, \quad R_F(N) \equiv \frac{Q_F(N+2)}{Q_F(N)}, \quad R_m(N) \equiv \frac{Q_0(N)}{Q_1(N)} \quad (49)$$

for large $N = \mathcal{O}(1000)$. Here we discuss how the transfer matrix elements in eq.(12) can be constructed using these ratios while avoiding arithmetic over- or underflow.

First we note that for the calculation of the mass gaps or expectation values, the overall normalisation of the transfer matrices is not relevant, as long as all matrices are normalised consistently. We can therefore rescale all matrix elements by a constant factor, e.g., $Q_1(0)$ which is of order $\mathcal{O}(1)$. The contribution of the site weight to the matrix elements then becomes $Q_F(N)/Q_1(0)$ and this can be evaluated as

$$\frac{Q_F(N)}{Q_1(0)} = R_m(0)^{1-F} \cdot \prod_{n=0}^{N-1} R'_F(n). \quad (50)$$

In case the ratios R'_F are ill-defined, e.g. when employing the superpotential P_u for which only $N = 0 \pmod 2$ is allowed, they are replaced by $R_F(n)$ and the product runs up to $N-2$. Even when the ratios R'_F or R_F are $\mathcal{O}(1)$ the product can lead to arithmetic overflow when N is $\mathcal{O}(1000)$. In that case it is advisable to evaluate the product logarithmically, i.e., as

$$\ln \prod_n R'_F(n) = \sum_n \ln R'_F(n) \quad (51)$$

and analogously for R_F .

In addition, the factorials in eq.(12) may lead to arithmetic underflow when n_i^b or m_i^b is $\mathcal{O}(300)$. Also in this case it is advisable to calculate the factorials logarithmically,

$$\ln \sqrt{\frac{1}{n_i^b!}} = -\frac{1}{2} \sum_{n=0}^{n_i^b} \ln n, \quad (52)$$

and possibly combine the result with the one from eq.(51) before exponentiating. Finally, it is important to note that the logarithmic sums should be chosen only when the over- or underflow de facto occurs, as otherwise the loss of precision in eq.(51) and (52) might be sufficient to yield inaccurate results.

References

- [1] D. Baumgartner and U. Wenger, *Supersymmetric quantum mechanics on the lattice: I. Loop formulation*, *Nucl.Phys.* **B894** (2015) 223–253, [[arXiv:1412.5393](#)].
- [2] J. Giedt, R. Koniuk, E. Poppitz, and T. Yavin, *Less naive about supersymmetric lattice quantum mechanics*, *JHEP* **0412** (2004) 033, [[hep-lat/0410041](#)].
- [3] G. Bergner, T. Kaestner, S. Uhlmann, and A. Wipf, *Low-dimensional Supersymmetric Lattice Models*, *Annals Phys.* **323** (2008) 946–988, [[arXiv:0705.2212](#)].
- [4] S. Catterall and E. Gregory, *A Lattice path integral for supersymmetric quantum mechanics*, *Phys.Lett.* **B487** (2000) 349–356, [[hep-lat/0006013](#)].
- [5] D. Baumgartner and U. Wenger, *Supersymmetric quantum mechanics on the lattice: III. Simulations and algorithms*, *Nucl. Phys.* **B899** (2015) 375–394, [[arXiv:1505.07397](#)].
- [6] D. Baumgartner, *Supersymmetric Models in Low Dimensions on the Lattice*. PhD thesis, AEC for fundamental physics, University of Bern, 2012.
- [7] K. Steinhauser and U. Wenger, *Spontaneous supersymmetry breaking in the two-dimensional $N=1$ Wess-Zumino model*, *Phys.Rev.Lett.* **113** (2014) 231601, [[arXiv:1410.6665](#)].
- [8] A. Salam and J. Strathdee, *On goldstone fermions*, *Physics Letters* **B49** (1974), no. 5 465 – 467.
- [9] C. Wozar and A. Wipf, *Supersymmetry breaking in low dimensional models*, *Annals Phys.* **327** (2012) 774–807, [[arXiv:1107.3324](#)].
- [10] I. Kanamori, F. Sugino, and H. Suzuki, *Observing dynamical supersymmetry breaking with Euclidean lattice simulations*, *Prog.Theor.Phys.* **119** (2008) 797–827, [[arXiv:0711.2132](#)].
- [11] I. Kanamori, *A Method for Measuring the Witten Index Using Lattice Simulation*, *Nucl.Phys.* **B841** (2010) 426–447, [[arXiv:1006.2468](#)].
- [12] M. Hanada, J. Nishimura, and S. Takeuchi, *Non-lattice simulation for supersymmetric gauge theories in one dimension*, *Phys.Rev.Lett.* **99** (2007) 161602, [[arXiv:0706.1647](#)].
- [13] N. V. Prokof'ev and B. V. Svistunov, *Worm algorithms for classical statistical models*, *Phys.Rev.Lett.* **87** (2001) 160601, [[cond-mat/0103146](#)].
- [14] U. Wenger, *Efficient simulation of relativistic fermions via vertex models*, *Phys.Rev.* **D80** (2009) 071503, [[arXiv:0812.3565](#)].

- [15] S. Chandrasekharan, *The Fermion bag approach to lattice field theories*, *Phys.Rev.* **D82** (2010) 025007, [[arXiv:0910.5736](#)].
- [16] S. Chandrasekharan, *Solutions to sign problems in lattice Yukawa models*, *Phys.Rev.* **D86** (2012) 021701, [[arXiv:1205.0084](#)].
- [17] S. Chandrasekharan, *Fermion Bag Approach to Fermion Sign Problems*, *Eur.Phys.J.* **A49** (2013) 90, [[arXiv:1304.4900](#)].
- [18] K. Steinhauser and U. Wenger, *Loop formulation of supersymmetric Yang-Mills quantum mechanics*, *JHEP* **1412** (2014) 044, [[arXiv:1410.0235](#)].
- [19] V. Maillard and U. Wenger, *Worm algorithm for the $O(2N)$ Gross-Neveu model*, *PoS LAT2010* (2010) 257, [[arXiv:1104.0569](#)].
- [20] K. Steinhauser and U. Wenger, *Loop formulation of the supersymmetric nonlinear $O(N)$ sigma model*, *PoS LATTICE2013* (2013) 092, [[arXiv:1311.5403](#)].
- [21] D. Baumgartner and U. Wenger, *Simulation of supersymmetric models on the lattice without a sign problem*, *PoS LAT2010* (2011) [[arXiv:1104.0213](#)].